Additive Manufacturing 105 (2025) 104770

Contents lists available at ScienceDirect

Additive Manufacturing

journal homepage: www.elsevier.com/locate/addma

Research paper

Direct ink writing of magnetic soft materials with optimized printing path

Chao Wang [a], Zhi Zhao [a], Zeyu Li [a], Yingqi Jia [a], Arvin Ardebili Sharma [b], Xiaojia Shelly Zhang [a,c,d,*]

[a] Department of Civil and Environmental Engineering, University of Illinois Urbana-Champaign, Urbana, IL 61801, USA
[b] Department of Materials Science and Engineering, University of Illinois Urbana-Champaign, Urbana, IL 61801, USA
[c] Department of Mechanical Science and Engineering, University of Illinois Urbana-Champaign, Urbana, IL 61801, USA
[d] National Center for Supercomputing Applications, Urbana, IL 61801, USA

ARTICLE INFO

Keywords:
Direct ink writing
Topology optimization
Toolpath generation
Continuous magnetization
Magnetic soft material

ABSTRACT

Direct ink writing (DIW) of magnetically responsive soft materials with high remanent magnetization, where a locally applied magnetic field aligns magnetized particles along the printing path, offers transformative potential across diverse applications. However, most existing studies have been confined to the printing of discrete magnetization patterns, which could restrict the functionality of achievable designs and preclude the creation of continuous magnetization distributions. Moreover, there is a lack of effective and automated path-generation methods capable of translating numerical designs with heterogeneous magnetization distributions and complex geometries into precise, manufacturable toolpaths. In this work, we introduce a novel, comprehensive framework that seamlessly integrates optimized design and additive manufacturing of hard-magnetic soft materials, enabling continuous magnetization encoding through the automatically generated printing paths. The framework extend the magneto-active soft material optimization approach to generate printable designs with continuous magnetization while considering manufacturing constraints. We propose an efficient toolpath generation algorithm that maps optimized magnetization directions to continuous printing paths, preserving the optimized topology. We explain the DIW process and experimentally characterize the mechanical and magnetic properties of the fabricated materials. The capabilities of the framework are comprehensively demonstrated through three experimentally validated examples: a magneto-active elevator mechanism, butterfly metasurfaces with complex magnetization distributions encoded by corresponding toolpaths, and a metamaterial design with globally generated toolpaths. These examples showcase the framework's capability to effectively bridge the gap between design and additive manufacturing. The framework also has the potential for generalization across emerging 3D and 4D printing technologies involving other functional materials, opening new frontiers in the design and manufacturing of intelligent, responsive material systems.

1. Introduction

Direct ink writing (DIW) is a versatile 3D printing technique that uses a computer-controlled gantry system to extrude material ink under pressure, constructing structures layer by layer [1–4]. This method is straightforward to implement, offering flexibility in material selection, efficient raw material usage, and high customizability in the printing process. Due to these advantages, DIW has been employed to print a range of functional materials capable of shape transformation in response to stimuli, including shape memory polymers (SMPs) [5–7], liquid crystal elastomers (LCEs) [8–11], hydrogels [12–14], and magneto-active materials [2,15–18], demonstrating significant potential in biomedical, electronic, soft robotics, and actuator applications.

In this study, we focus on the DIW of hard-magnetic soft material, where the ink is prepared by mixing the hard-magnetic particles (*e.g*, NdFeB microparticles) with the soft material matrix [15,16,19,20]. The high coercivity of the hard-magnetic particles allows it to retain a strong remnant magnetization once magnetized. The magnetized NdFeB microparticles are initially randomly distributed in the ink composites. During the DIW process, the magnetized particles are reoriented by a locally applied magnetic field at the printing location, creating a certain direction of magnetization in the printed filaments that aligns with the printing path (see Fig. 1). This DIW-induced magnetization opens a new avenue for the fabrication of hard-magnetic soft material with complex magnetization distributions to achieve fast shape transformation under magnetic stimulation. Compared to traditional mold-casting approaches [21–24], DIW enables seamless transitions between different magnetization directions, eliminating the need for

* Corresponding author.
E-mail address: zhangxs@illinois.edu (X.S. Zhang).

https://doi.org/10.1016/j.addma.2025.104770
Received 8 December 2024; Received in revised form 16 March 2025; Accepted 31 March 2025
Available online 12 April 2025

post-bonding separate components with distinct magnetizations. As a result, DIW has been widely adopted in many studies to fabricate intuitively [15] or inversely [19,20,25] designed hard-magnetic soft materials with heterogeneous magnetization distributions.

However, existing work on DIW-printed hard-magnetic soft materials has primarily been limited to discrete magnetizations, with most relying on commercial software to slice the printing path to align with the magnetization [15,16,19,20]. The limited selection of magnetization orientations in these discrete designs does not support the realization of a continuous magnetization distribution, which can constrain the achievable performance space. Furthermore, the sharp transitions between discrete magnetizations may lead to significant self-interactions, potentially disrupting performance. Also, when parts are printed separately in a discrete way, the interfaces between them may exhibit reduced bonding strength. Regarding these limitations, this work aims to enable the DIW of hard-magnetic soft materials with continuously varying magnetization and complex geometries while developing an efficient path generation algorithm to seamlessly translate numerical designs into printable toolpaths.

In our recent work [26], we introduced a topology optimization framework for designing hard-magnetic soft materials with continuous magnetization orientations, which are suited for DIW fabrication. Nonetheless, bridging the gap between topology-optimized designs [27,28] and physical products, as well as conducting experimental validation, presents several challenges. These include integrating realistic manufacturing constraints into the design framework, accurately characterizing material properties, and most critically, generating a continuous printing path that aligns with the optimized voxelized magnetization orientations while maintaining the optimized geometric features.

To address the challenge of path generation, we draw inspiration from stress field-dependent toolpath generation methods used in the 3D printing of continuous fiber-reinforced composites, where paths are aligned with stress flow directions [29–31]. There are two primary approaches to this type of toolpath generation: explicit and implicit methods. In the explicit method, the toolpath is iteratively advected using a streamline tracing technique that follows the target orientation field [29,30]. This approach is straightforward to implement and ensures perfect alignment with the target magnetization direction. However, it requires interpolating the target vector field and solving the advection equations iteratively at each point. Computational time is influenced by factors including the domain size, step length, path length, and path spacing. As a result, this method can become computationally expensive for large domains with higher-resolution paths and finer spacing. In contrast, the implicit method converts orientation information into a global scalar field, with toolpaths generated along the isovalue lines of this field [31]. The computational time for this method is independent of domain size, path spacing, and path resolution. The underlying principle of this implicit method, known as global parameterization, is widely applied in areas such as mesh generation [32,33] and the dehomogenization of multi-scale topologies [34,35], where it has demonstrated stability and computational efficiency. These strategies offer valuable insights for generating toolpaths in hard-magnetic soft materials with optimized continuous magnetizations.

In this work, we develop a holistic framework that integrates optimized design with additive manufacturing (*i.e.*, DIW) of hard-magnetic soft materials and conduct comprehensive experimental demonstrations on optimized designs with various functionalities (see Fig. 1 and Movie S1 for the DIW process, path generation, fabrication, and experimental demonstrations). The key contributions of this study include: (1) **Extended numerical design methodology.** The topology optimization framework developed in [26] for continuous magnetization distribution is tailored to incorporate manufacturing constraints and extended to metasurface design, enabling 3D out-of-plane deformations, which broadens the design space and is particularly suited for the layer-by-layer DIW of planar structures. (2) **Efficient and universal path generation.** We develop a robust toolpath generation method based on the global parameterization to map the optimized continuous magnetization of hard-magnetic soft materials with complex geometries to the printing path. This approach ensures computational efficiency and precise alignment with the magnetization orientation. The approach also benefits the printing of other optimized path-dependent materials, such as continuous fiber-reinforced polymer composites and LCEs [36–38]. (3) **Effective experimental validation.** We fabricate the optimized designs using continuous printing paths aligned with the magnetization direction. The detailed DIW procedure and key printing parameters are discussed. Comprehensive material characterization, including the mechanical and magnetic properties of the printed hard-magnetic soft materials, is provided. The experimental results validate the successful realization of the intended actuation performance. To demonstrate the effectiveness of the framework, we present a magneto-active elevator design, a "butterfly" metasurface with different slicing toolpaths (magnetization distributions) to achieve various out-of-plane deformations, and a metamaterial design with an integrally generated toolpath for area minimization functionality.

The remainder of the paper is structured as follows. Section 2 introduces the numerical design method of the DIW-fabricable hard-magnetic soft material with continuous magnetizations. Section 3 introduces the toolpath generation algorithm. Section 4 describes the DIW process and material characterization. Section 5 presents demonstration examples, and Section 6 provides concluding remarks. The Appendix A outlines the energy interpolation scheme used in the optimization framework, and Appendix B provides the experimental measurement of the material's rheological properties and a reference for the optimal viscosity range that supports both particle alignment and printability.

2. Design method of DIW-fabricable hard-magnetic soft materials

This section presents a density-based topology optimization design method based on our previous work [26]. The goal is to optimize geometry and continuous remanent magnetization orientation to generate magnetic soft materials with desired functionalities. As shown in Fig. 2, the design method is tailored to satisfy the key design criteria essential for successful DIW fabrication:

(a) Allow arbitrary element-wise remanent magnetization orientations,
(b) Maintain a nearly uniform remanent magnetization magnitude,
(c) Ensure smooth spatial continuity of remanent magnetization,
(d) Ensure sufficiently large and well-defined members.

With these fabrication considerations, we present an optimization formulation for generating designs. The magneto-mechanical interpolated free energy model and associated finite element analysis are provided in Appendix A.

2.1. Parameterization of remanent magnetization

To satisfy criterion **a**, the element-wise residual magnetic flux density (linearly depending on the remanent magnetization through $\mathbf{M}_{\mathrm{r},e} = (1/\mu_0)\mathbf{B}_{\mathrm{r},e}$, where μ_0 is the magnetic permeability) is interpolated using two orthogonal base vectors, $\mathbf{B}_{\mathrm{r}}^{(1)}$ and $\mathbf{B}_{\mathrm{r}}^{(2)}$, for 2D designs, as follows:

$$\mathbf{B}_{\mathrm{r},e} = \overline{m}_e^{(1)}\mathbf{B}_{\mathrm{r}}^{(1)} + \overline{m}_e^{(2)}\mathbf{B}_{\mathrm{r}}^{(2)}, \tag{1}$$

where $\overline{m}_e^{(1,2)}$ is the element-wise physical magnetization variable.

To satisfy criterion **b**, we constrain the upper bound of the magnetization magnitude (the lower bound constraint is imposed in Formulation (5)) and apply an iso-parametric mapping scheme [39], ensuring $(\overline{m}_e^{(1)})^2 + (\overline{m}_e^{(2)})^2 \leq 1$. The mapping expression is given by

$$\begin{array}{l} \overline{m}_e^{(1)} = \sum_{i=1}^{8} a_i^{(1)} N_i(\overline{\xi}_e^{(1)}, \overline{\xi}_e^{(2)}) \\ \overline{m}_e^{(2)} = \sum_{i=1}^{8} a_i^{(2)} N_i(\overline{\xi}_e^{(1)}, \overline{\xi}_e^{(2)}) \end{array}, \tag{2}$$

where $N_i(\cdot)$ is the mapping function [39], inspired by the eight-node biquadratic quadrilateral element; $a_i = \{a_i^{(1)}, a_i^{(2)}\}^{\mathrm{T}}, i = 1 \ldots 8$ is the

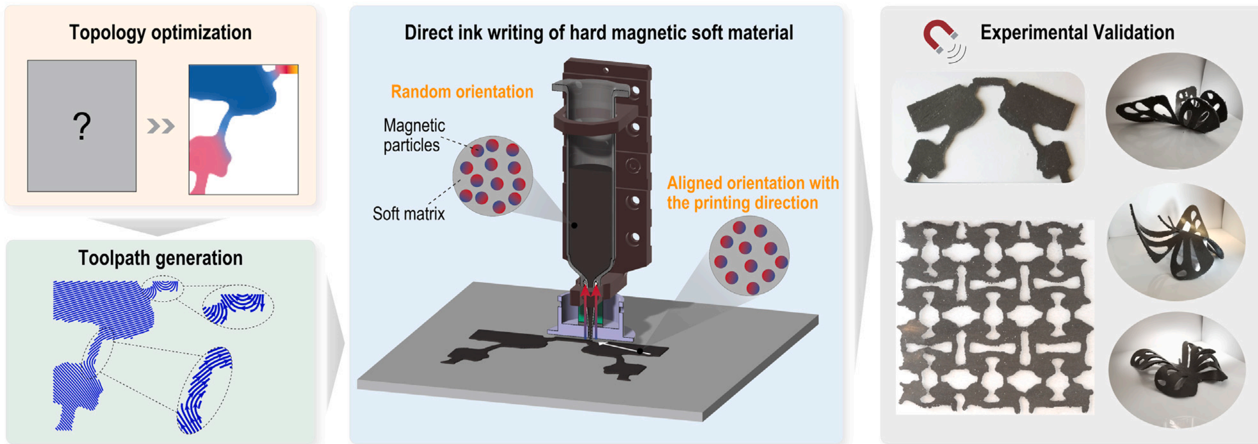

Fig. 1. Direct ink writing of hard-magnetic soft material with optimized continuous magnetization and experimental validation. See Movie S1 for the DIW process, path generation, fabrication, and experimental demonstrations.

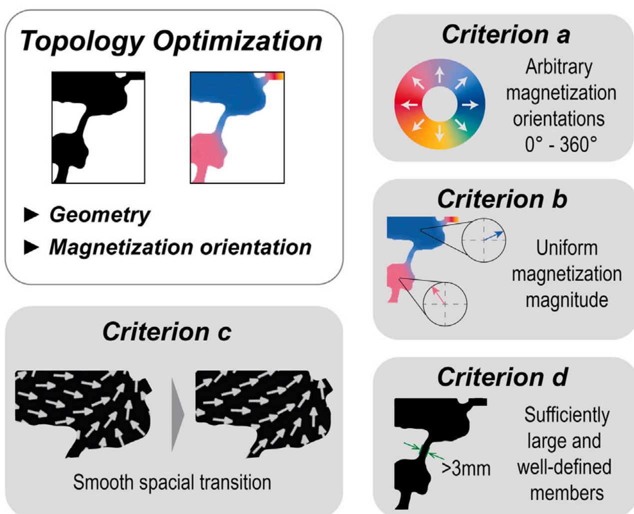

Fig. 2. Topology optimization design method and four key criteria for successful DIW fabrication.

coordinate of the ith node after mapping; $\bar{\xi}_e^{(1,2)}$ is the element-wise intermediate design variable with the range of $[-1, 1]$.

To satisfy criterion **c**, we enforce spatial continuity by filtering $\bar{\xi}_e^{(1,2)}$ using a distance-based filter [40], promoting smooth magnetization flow, as shown below:

$$\tilde{\xi}_e^{(j)} = \frac{\sum_{i\in\mathcal{I}_e(R_m)} w_m^{(i,e)} v_i \xi_i^{(j)}}{\sum_{i\in\mathcal{I}_e(R_m)} w_m^{(i,e)} v_i}, \quad j = 1, 2, \tag{3}$$

where $\xi^{(1,2)}$ represents the magnetization design variables, $\mathcal{I}_e(R_m)$ is the eth element set within a circle of radius R_m centered at the eth element centroid, v_i is the ith element volume, and the weight $w_m^{(i,e)}(R_m)$ is based on the distance between centroids $\mathbf{X}_i$ and $\mathbf{X}_e$, defined as $w_m^{(i,e)} = 1 - \left|\mathbf{X}_i - \mathbf{X}_e\right| / R_m$.

2.2. Parameterization of geometry

To satisfy criterion **d**, which ensures well-defined and discrete design regions, the physical density variable $\bar{\rho}_e$ (where $\bar{\rho}_e = 1$ represents a solid and $\bar{\rho}_e = 0$ denotes a void) is calculated using a Heaviside projection [41]:

$$\bar{\rho}_e = \frac{\tanh(\frac{\beta_\rho}{2}) + \tanh(\beta_\rho(\tilde{\rho}_e - \frac{1}{2}))}{2\tanh(\frac{\beta_\rho}{2})}, \tag{4}$$

where the parameter β_ρ controls the sharpness of the projection, $\bar{\rho}_e$ denotes the physical design variable, and the variable $\tilde{\rho}_e$ acts as an intermediate stage in the process.

Furthermore, to fulfill criterion **d**, which ensures sufficiently large member sizes, a filtering process is applied to the design variable ρ_e to compute the intermediate variable $\tilde{\rho}_e$. This filtering employs a distance-based method, similar to Eq. (3), to enforce a minimum feature size [42].

2.3. Optimization formulation

Leveraging the parameterization of the design space, we present a topology optimization formulation creating DIW-compatible magnetic designs with smoothly varying magnetization orientations. For load case ℓ, the design is subjected to an external magnetic field $\mathbf{B}_a^{(\ell)}$. The topology optimization problem is defined as follows:

$$\begin{aligned}
&\min_{\boldsymbol{\rho},\boldsymbol{\xi}^{(1)},\boldsymbol{\xi}^{(2)}} : J\left(\mathbf{u}^{(\ell)}\right), \quad \ell \in 1,\ldots,N_\ell; \\
\text{s.t.:}\quad & \frac{\mathbf{v}^{\mathrm{T}}\bar{\boldsymbol{\rho}}}{|\Omega_{\mathrm{h}}|} \le v_{\max}, \\
& \frac{\sum_{e=1}^{N_e}\left[\bar{\rho}_e\left(1-\left(1-\sqrt{(\overline{m}_e^{(1)})^2+(\overline{m}_e^{(2)})^2}\right)^{p_v}\right)\right]}{\sum_{e=1}^{N_e}\bar{\rho}_e} \ge 1-\bar{\varepsilon}_v, \\
& \left\{\sum_{e=1}^{N_e}\left[\frac{w_{\bar{\sigma}}(\bar{\rho}_e)}{v_e}\int_{\Omega_{\mathrm{h},e}}\bar{\sigma}_{\mathrm{VM}}\left(\bar{\boldsymbol{\sigma}}_{\mathrm{E}}(\mathbf{u}^{(\ell)})\right)\mathrm{d}\mathbf{X}\right]^{p_n}\right\}^{1/p_n} \le \bar{\sigma}_{\max}^{(\ell)}, \quad \ell = 1,\ldots,N_\ell, \\
& \mathbf{r}(\bar{\boldsymbol{\rho}},\overline{\mathbf{m}}^{(1)},\ldots,\overline{\mathbf{m}}^{(N_m)},\mathbf{u}^{(\ell)}) = \mathbf{0}, \quad \ell = 1,\ldots,N_\ell, \\
& \mathbf{0} \le \boldsymbol{\rho} \le \mathbf{1}, \\
& -\mathbf{1} \le \boldsymbol{\xi}^{(1,2)} \le \mathbf{1}.
\end{aligned} \tag{5}$$

In this formulation, the displacement vector for load case ℓ, denoted as $\mathbf{u}^{(\ell)}$. The optimization process aims to minimize an objective function, $J(\mathbf{u}^{(\ell)})$, which depends on $\mathbf{u}^{(\ell)}$ and is problem-specific. A volume constraint is imposed, where $\mathbf{v}$ represents the element volume vector, and $v_{\max}$ defines the maximum allowable volume ratio. The equilibrium condition $\mathbf{r} = \mathbf{0}$ is treated as a nested constraint.

To satisfy criterion **b**, a lower bound on magnetization magnitude is applied alongside the isoparametric mapping (Eq. (2)), ensuring

$\sqrt{\left(\overline{m}_e^{(1)}\right)^2 + \left(\overline{m}_e^{(2)}\right)^2}$ is close to 1 [39]. Here, $p_v \geq 1$ is a penalty factor, and $\overline{\epsilon}_v$ is a small value introduced for numerical stability.

To address criterion **d** of mitigating the formation of thin members, stress constraints are incorporated to ensure the von Mises stress $\overline{\sigma}_{\mathrm{VM}}$, obtained from the Cauchy stress tensor $\overline{\sigma}_{\mathrm{E}}$ [43], remains below a prescribed limit, $\overline{\sigma}^{(\ell)}_{\max}$. A relaxation approach, $w_{\overline{\sigma}}(\overline{\rho}_e) = \epsilon + (1-\epsilon)\overline{\rho}_e^{-q_\rho}$ ($q_\rho < 1$), is used to prevent singularities, with stress estimated via the p-norm method with the parameter of p_n.

Sensitivities are computed using the adjoint method [42]. The Method of Moving Asymptotes (MMA) [44] is employed to solve the gradient-based optimization problem.

3. Toolpath generation method

After obtaining the optimized design, which includes element-wise density and magnetization vector information, we introduce the process of mapping this design to physical toolpaths suitable for DIW. Fig. 3 illustrates the proposed toolpath generation method step by step. The method comprises three main steps: global parameterization (Fig. 3a–c), toolpath extraction (Fig. 3d–f), and postprocessing (Fig. 3g).

3.1. Global parameterization

The key to DIW of hard-magnetic soft materials is aligning the toolpath with the optimized magnetization direction ($\mathbf{M}_{\mathrm{r}}$) to achieve the desired actuation deformation under an external magnetic field. Inspired by field alignment algorithms for carbon fiber placement [31] and mesh generation [32,33], we adopt a global parameterization strategy as follows.

We begin by binarizing the optimized design into purely solid ($\overline{\rho}_e = 1$) and void ($\overline{\rho}_e = 0$) regions to ensure physical consistency (Fig. 3a). We then extract the mesh information of the discrete design, including nodes, elements, element-wise density, and magnetization direction ($\mathbf{M}_{\mathrm{r}}$). Finally, we define a dimensionless scalar field, $v(\mathbf{X})$, within the solid domain (Ω_{s}) and construct an orientation energy ($E_{\mathrm{orient}}(v)$) as

$$E_{\mathrm{orient}}(v) = \int_{\Omega_{\mathrm{s}}} \|w\nabla v - \mathrm{rot}^{+}(\mathbf{M}_{\mathrm{r}})\|^2 \mathrm{d}\mathbf{X}. \quad (6)$$

Here, the operator rot^{+} rotates the target magnetization direction counterclockwise by $\pi/2$ (Fig. 3b), and $w > 0$ is a prescribed spacing parameter. Note that $E_{\mathrm{orient}}(v)$ applies only to the solid part of the discrete design (Fig. 3c).

After defining the orientation energy ($E_{\mathrm{orient}}(v)$), our goal is to determine its minimizer ($v^{*}(\mathbf{X})$) such that $w\nabla v^{*}(\mathbf{X}) = \mathrm{rot}^{+}(\mathbf{M}_{\mathrm{r}}(\mathbf{X}))$. Mathematically, this relationship ensures that the gradient of the scalar field $v(\mathbf{X})$ is collinear with the perpendicular direction of $\mathbf{M}_{\mathrm{r}}$. Physically, the contour lines of $v(\mathbf{X})$ align with the target magnetic magnetization direction ($\mathbf{M}_{\mathrm{r}}$).

To compute $v^{*}(\mathbf{X})$, we derive the gradient of $E_{\mathrm{orient}}(v)$ as

$$g(v) = \frac{\mathrm{d}E_{\mathrm{orient}}(v)}{\mathrm{d}v}$$

and then solve $g(v) = 0$. For definiteness, we set $v(\mathbf{X}_0) = 0$ for a dummy $\mathbf{X}_0 \in \Omega_{\mathrm{s}}$. To further solve $g(v) = 0$, we discretize it into the matrix form using finite element analysis in FEniCSx [27,45]. Finally, we compute $v^{*}(\mathbf{X})$ at element vertices (Fig. 3c), which will be used for toolpath extraction as introduced below.

3.2. Toolpath extraction

After obtaining the scalar field, $v^{*}(\mathbf{X})$, we extract its iso-value contours using the "`tricontour`" function from "`matplotlib`" (Fig. 3d). The extracted contour lines, $\mathcal{S}$, are collections of line segments, where each segment s_i is defined by two points, (x_1, y_1) and (x_2, y_2). Additionally, the spacing of these contour lines can be adjusted by modifying the level intervals within the "`tricontour`" function.

Note that "`tricontour`" defines the extracted contour lines on a different triangular grid, $\mathcal{M}$, which is mapped from the solid domain (Ω_{s}). This mapping introduces redundant regions that need to be removed (Fig. 3d). To address this issue, we evaluate the midpoint of each line segment to determine whether it lies within the solid domain (Ω_{s}), and any segments outside Ω_{s} are eliminated to form consistent design geometries (Fig. 3e).

In contrast to the bi-directional nature of fiber orientation, where performance remains consistent between directions differing by an angle of π, the direction of remanent magnetization is inherently unidirectional. Consequently, for each line segment s_i, we compare the cosine similarities between the two possible orientations $\mathbf{r}$ and $-\mathbf{r}$, with the optimized magnetization direction $\mathbf{M}_{\mathrm{r},e}$, as shown in Fig. 3(f). The start and end points of the line segment are then adjusted in the direction that exhibits the higher cosine similarity.

3.3. Postprocessing

After obtaining the toolpath set $\mathcal{S}$ with the corrected directions, we perform several postprocessing procedures to meet practical printing requirements and enhance print quality. These procedures include adjusting the minimum length of the toolpaths, tuning the resolution, ordering the printing sequence, and converting the format for printing (see Fig. 3g).

First, toolpaths that are excessively short are generally unnecessary and undesirable for printing. Thus, the length L of each individual toolpath is calculated by summing the lengths of its constituent line segments. Toolpaths shorter than a specified minimum length $L < L_{\min}$ are removed to ensure the quality of the final printed product.

Second, the resolution, which defines the number of line segments within each toolpath, is adjusted to balance printing quality and printer storage/memory usage. A finer resolution enhances the smoothness of the printed path and ensures high-precision alignment. In contrast, a coarser resolution reduces data storage requirements and memory usage for the printing system, which is particularly advantageous for large-scale prints with dense toolpaths and fine path widths. Adjustments to the minimum toolpath length and resolution remain optional and can be tailored to specific printing needs.

Furthermore, the printing sequence of the toolpaths is optimized to enhance printing efficiency and quality. This is achieved by formulating a traveling salesman problem (TSP) and approximating a solution using a nearest neighbor algorithm. Initially, a random toolpath is selected. Subsequently, the nearest remaining toolpaths are chosen iteratively until all toolpaths are visited. Two strategies are considered for determining the nearest toolpath: (1) based on the distance between the end point $\mathbf{X}_{\mathrm{end}}$ of the current toolpath and the start point $\mathbf{X}_{\mathrm{start}}$ of the remaining toolpaths, denoted as d_{e-s}; and (2) based on the distance between the start point of the current toolpath and the start point of the remaining toolpaths, denoted as d_{s-s}, as illustrated in Fig. 3g. Although the first strategy may minimize the total travel distance of the printing head, we prefer the second strategy in this work. This approach ensures that the subsequent toolpath is adjacent to the last printed one, promoting better adhesion of the printed material and facilitating quality monitoring.

Finally, the adjusted toolpath set $\mathcal{S}$ is converted into a format compatible with the printer, such as DXF or G-code. In this work, we use the Python library "`ezdxf`" to convert the toolpaths into the DXF format, which is compatible with our printing system. The generated toolpaths can also be modified to repeat along the z-axis for multi-layer designs.

4. Printing and material characterization of hard-magnetic soft materials

The effectiveness of DIW of hard-magnetic soft materials in achieving magnetically actuated deformation has been explored in [15]. In

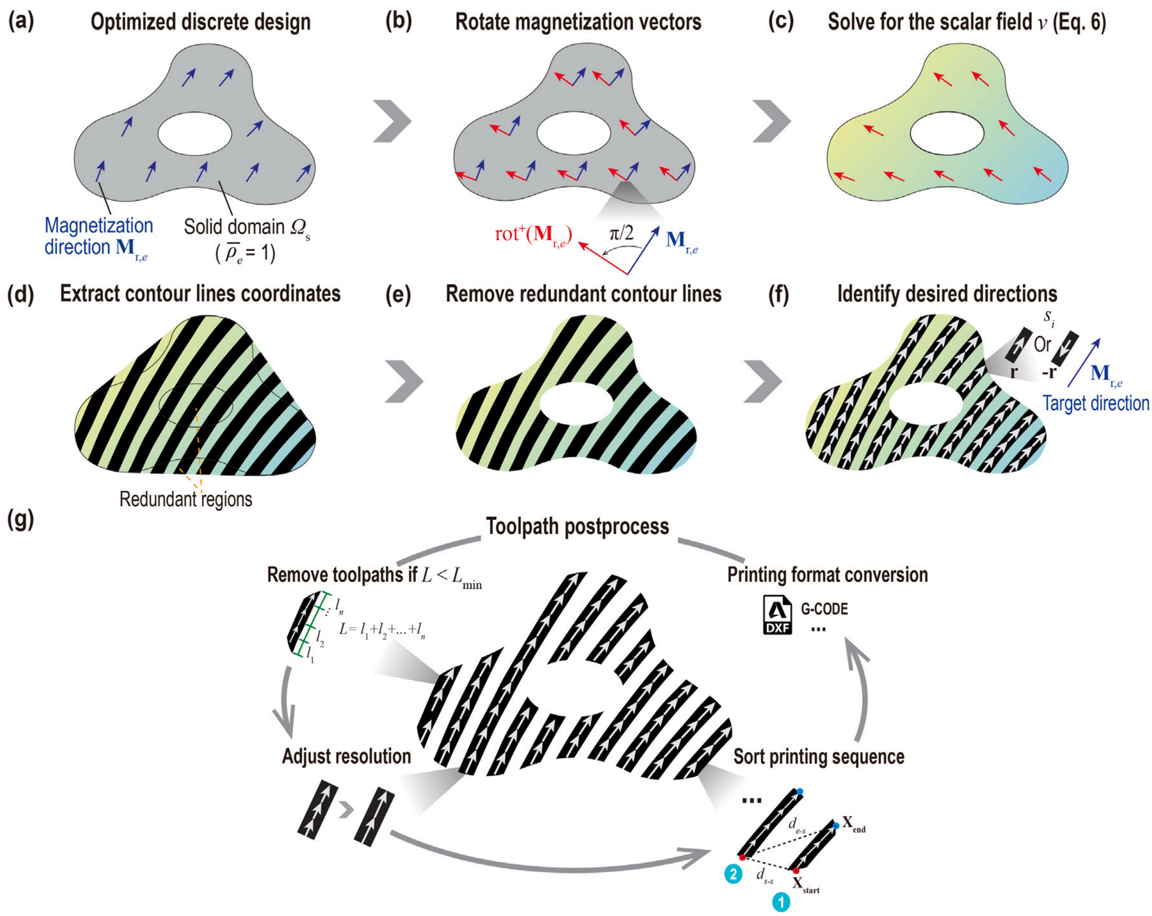

Fig. 3. Toolpath generation method. (a)–(c) Global parameterization. (d)–(f) Toolpath extraction. (g) Toolpath postprocessing.

this section, we present the detailed fabrication procedures for DIW of magnetic soft materials with topology-optimized printing paths, along with the material characterization of the mechanical and magnetic properties of the printed samples.

4.1. DIW of hard-magnetic soft materials

4.1.1. Printing setup

The DIW printer for hard-magnetic soft materials comprises a computer, 3-axis gantry system, material syringe, dispenser, permanent or electric magnet, magnetic shielding, and printing bed. The printing setup is shown in Fig. 4(a) and (b). The process begins with preparing the magnetic ink material and loading it into the syringe, followed by attaching printing tips of the desired dimensions. The magnetic ink material is then precisely dispensed using a computer-controlled gantry system that follows the optimized printing path. An air pressure-based dispenser (Nordson) is connected to the syringe to extrude the material at the desired pressure. A permanent magnet (R841) is affixed to the nozzle to realign the magnetic particles with the printing direction. Magnetic shielding is applied to prevent the magnet from influencing the printed samples. The magnetic field generated at the printing tip by the permanent magnet is measured as 40 mT, while the measured value after shielding is less than 0.4 mT. This combination is proven to be sufficient to reorient the magnetic particle direction as well as not perturb the printed material after shielding. A flat, smooth aluminum plate serves as the printing bed, ensuring no plastic deformation occurs under high temperatures.

4.1.2. Ink preparation

The magnetic ink is prepared through the following steps. First, PDMS (Dow Sylgard^{TM} 184 Silicone) base and Ecoflex 00-30 Part B are mixed in a 1:2 volume ratio. Fumed silica nanoparticles (average size 20 nm, 2 wt% relative to Ecoflex 00-30 Part B) are then added to adjust the ink's rheological properties, which is crucial for maintaining the printed material's shape and preventing overflow. The mixture is stirred at 2000 rpm for 2 min. Subsequently, NdFeB magnetic particles (average size 5 μm, 55 vol% relative to the PDMS base) are incorporated and mixed at 2000 rpm for 3 min, followed by a 1 min defoaming process to eliminate trapped bubbles. PDMS curing agent is then added at 10 vol% relative to the PDMS base and mixed at 2000 rpm for 1 min. The prepared mixture is first transferred into a syringe, which is then placed inside an impulse magnetizer (IM-10-30). A 2 T impulse magnetic field is applied to magnetize the embedded particles, ensuring that the NdFeB particles reach at least 95% magnetic saturation. In hard-magnetic soft materials, high remanent magnetization is retained even after the magnetizing field is removed. This remanent magnetization allows the orientation of embedded particles in the ink to be freely controlled by applying external magnetic fields with strengths far below the material's coercive strength. The syringe containing the magnetized ink is mounted onto the gantry system, with a permanent magnet and magnetic shield attached to the printing tip. As illustrated in Fig. 4(b), the magnetic particles embedded in the composite ink are reoriented by the magnetic field generated by the permanent magnet, aligning the magnetization of the printed filament with the printing direction. A detailed explanation and illustration of the magnetization and alignment process are provided in Section 4.1.4 and Fig. 5. During printing, the ink remains in a viscoelastic liquid state. The process

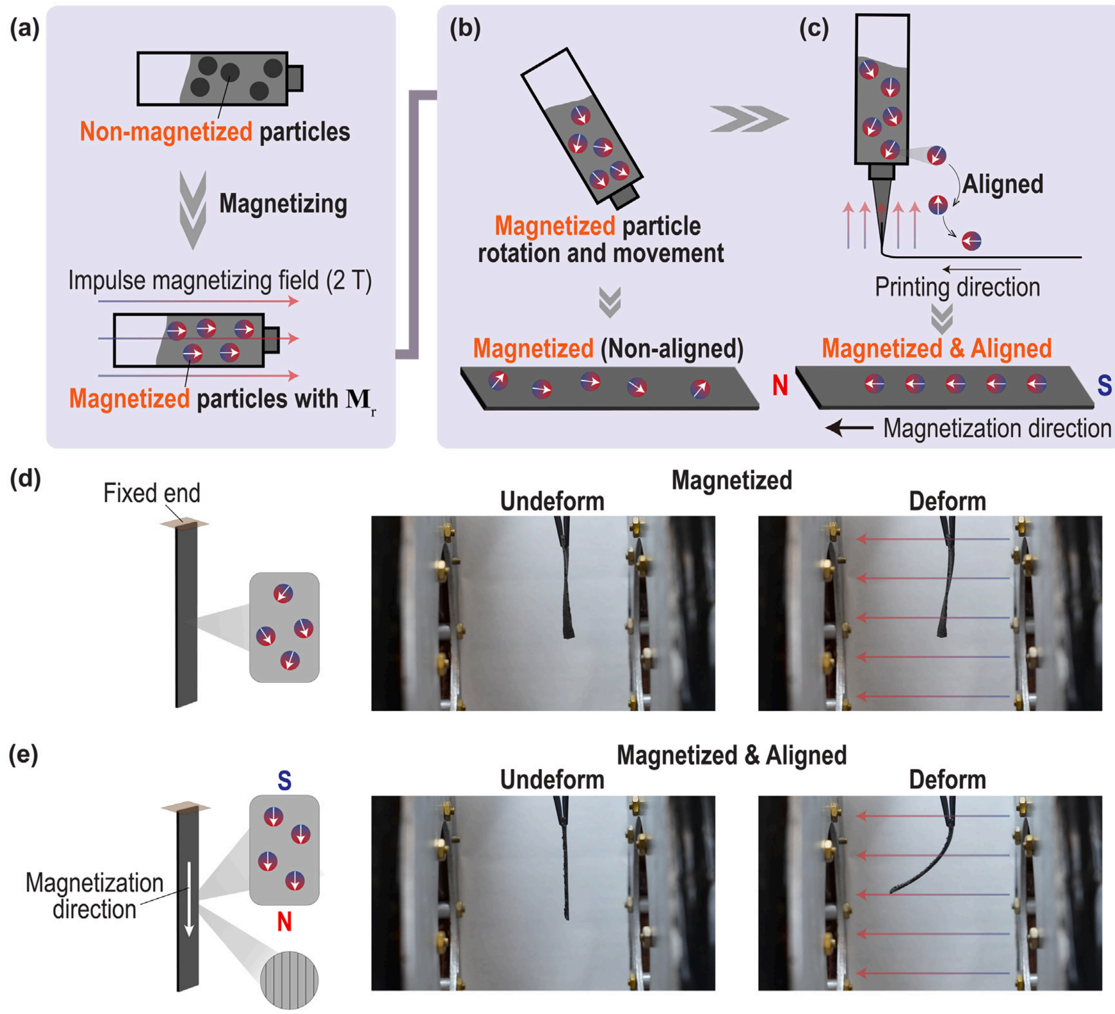

Fig. 4. DIW setup and material characterization of the printed hard-magnetic soft material. (a) Photograph of the DIW process for an optimized design. (b) Schematic illustrating the printing setup, which aligns the magnetization direction with the printing path. (c) Experimentally measured stress–strain curves (non-magnetized samples) for both horizontal and vertical printing paths under uniaxial tension. (d) Comparison of the experimentally measured (average) and fitted stress–strain curves. (e) Measured magnetic flux density of the sample at different angular positions (Sample size: 2 mm × 2 mm × 1 mm). (f) Measured magnetic hysteresis loop at θ = 180°.

window is defined by a viscosity low enough to enable particle rotation and smooth extrusion while being high enough to prevent excessive diffusion or settling. Based on our experimental observations, printing within 6 h after mixing ensures stable print quality, with extrusion pressure adjusted between 15–30 psi. The material's rheological properties, characterized in Appendix B, provide a reference for the optimal viscosity range that supports both particle alignment and printability.

4.1.3. Printing parameters

The corresponding DXF files generated by the path generation algorithm are loaded into the software to initiate the printing process. Prior to printing, a thin layer of Ease Release™ 200 demolding agent is sprayed on the printing bed to facilitate easy removal of the material afterward. Based on our experimental experience, the following printing parameters are employed to ensure consistently high-quality printed samples. The dispenser pressure is set at 15 psi to allow for smooth ink flow, with a printing speed of 5 mm/s. The shutoff distance and delay are adjusted to 0.15 mm and 0.3 s, respectively, to ensure clean transitions and sharp edges in the printed object. Nozzle tips with an inner diameter of 0.41 mm are used, and the toolpath spacing is also set at 0.41 mm to match the nozzle tip size. The height between the nozzle tip and the printing bed, as well as the layer lift height, are also set at 0.41 mm. Maintaining consistency in nozzle diameter, toolpath spacing, and printing height is crucial for achieving high-quality prints. In this work, three layers were printed for each sample. After printing, the material is cured at 212 °F for 1 h.

4.1.4. Magnetization and rearrangement of embedded magnetic particles in DIW

In this section, we provide an illustrative figure and a demonstration experiment to explain in detail how the magnetic particles are magnetized and aligned during the DIW process. As illustrated in Fig. 5(a), the non-magnetized particles are first magnetized to retain the remanent magnetization. After removing the impulse magnetizing field, since the ink remains in a viscoelastic liquid state, the magnetized particles can rotate and move during transportation (Fig. 5b). Consequently, a sample fabricated at this stage would exhibit randomly oriented magnetic dipoles. During printing (Fig. 5c), a magnetic field is applied near the nozzle tip. As the magnetized particles pass through this region, they experience magnetic torque, causing them to realign with the applied field. This results in a printed filament whose magnetization direction follows the printing path.

To validate this effect, we fabricated two samples (dimension: 49 mm × 10 mm × 1.5 mm) : one magnetized without alignment and another magnetized with alignment during printing. A demonstration experiment (Fig. 5d and e) was conducted to compare their responses under an out-of-plane magnetic field ($|\boldsymbol{B}_a|$ = 12 mT). The non-aligned sample exhibited limited and unpredictable deformation (Fig. 5d),

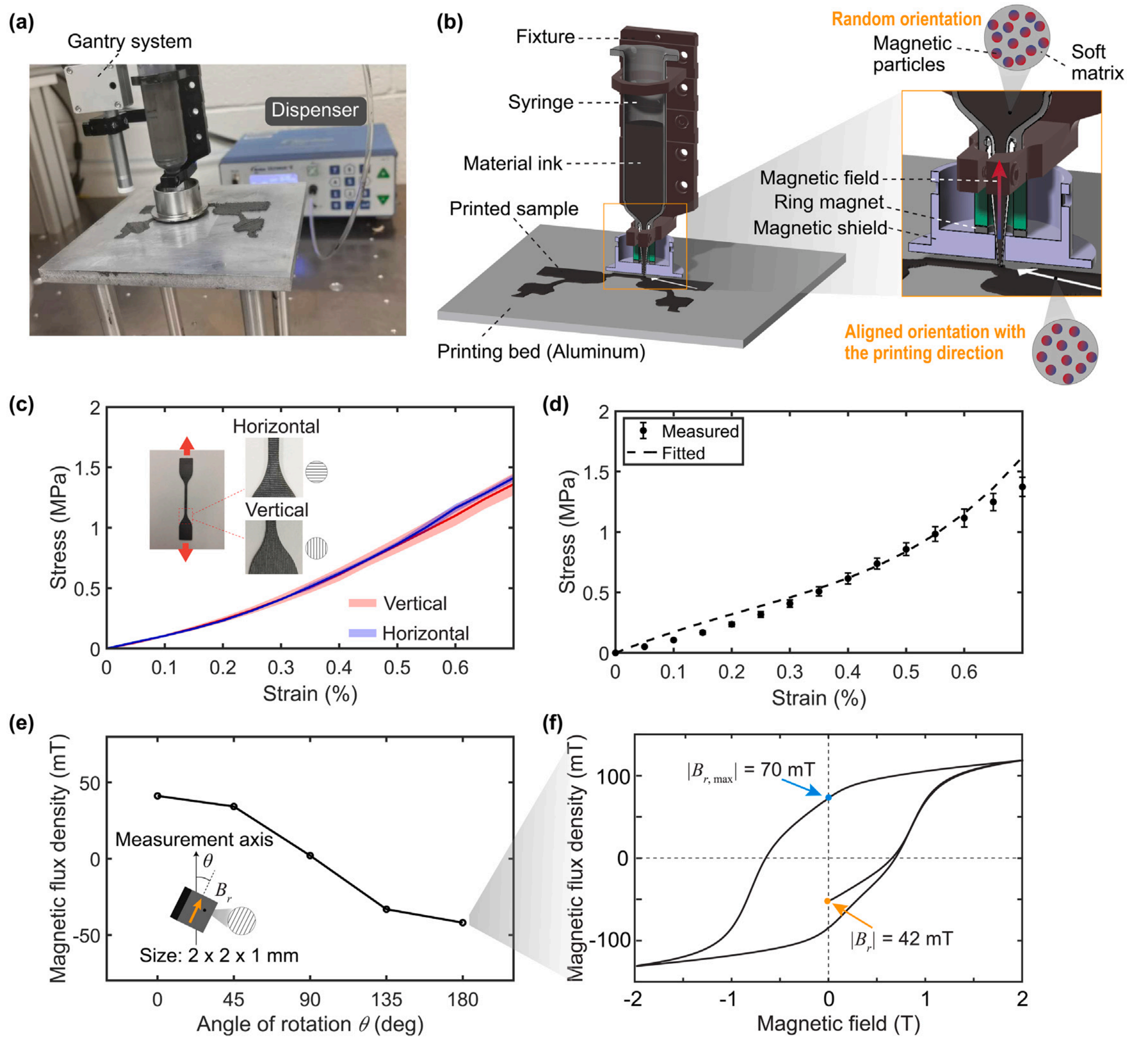

Fig. 5. Illustration of the particle rearrangement during the printing process. (a) Magnetizing process. (b) Magnetized sample without particle alignment. (c) Magnetized sample with particle alignment. (d) Magnetic actuation of the magnetized (non-aligned) sample. (e) Magnetic actuation of the magnetized and aligned sample.

whereas the aligned sample displayed bending deformation as the magnetization direction tend to align with the magnetic field direction (Fig. 5e).

4.2. Material characterization

To enable accurate modeling and numerical prediction of the DIW-printed hard-magnetic soft materials, it is essential to characterize their mechanical and magnetic properties.

4.2.1. Mechanical property of the DIW printed hard-magnetic soft material

For mechanical property characterization, non-magnetized dumbbell specimens were prepared via DIW in the absence of external magnetic field for uniaxial stretching tests. To investigate the potential path-dependent anisotropy induced by printing directions, specimens were printed with paths in both vertical and horizontal orientations, with three replicates for each group. To ensure uniformity, square sheets were printed first using a dispensing tip with an inner diameter of 0.41 mm at a printing speed of 5 mm/s. After curing, the sheets were cut into dumbbell specimens using a die, in accordance with the ASTM D412-16 standard [46]. Uniaxial tension tests were conducted using an Instron testing machine with the loading rate of 5 mm/min. The average stress–strain data is presented in Fig. 4(c). For the vertical printing path direction, the loading direction is parallel to the printing path, while for the horizontal printing path direction, the loading direction is perpendicular. The results show no significant difference between non-magnetized samples printed in the vertical and horizontal directions, suggesting that the printing direction does not induce significant anisotropy. The average data from both orientations were then fitted using an isotropic hyperelastic model [47] as shown in Eq. (7).

$$W_E\left(I_1(\boldsymbol{F})\right) = \sum_{r=1}^{2} \frac{3^{1-\alpha_r}}{2\alpha_r} \mu_r \left(I_1^{\alpha_r} - 3^{\alpha_r}\right), \tag{7}$$

where I_1 is the first invariant of $\boldsymbol{C} = \boldsymbol{F}^{\mathrm{T}}\boldsymbol{F}$ depending on deformation gradient $\boldsymbol{F}$. We observe that the measured data can be generally fitted well with the material constants $\alpha_1 = 5.0625$, $\alpha_2 = -4.7973$, $\mu_1 = 0.3326$ MPa, and $\mu_2 = 0.3039$ MPa (Fig. 4d). We note that the use of the hyperelastic model is motivated by its ability to predict mechanical behavior over a wide range of deformations, as well as its simple mathematical form, which facilitates derivation and implementation in our in-house code. We highlight that our design framework is general and allows for substitution with other models as needed.

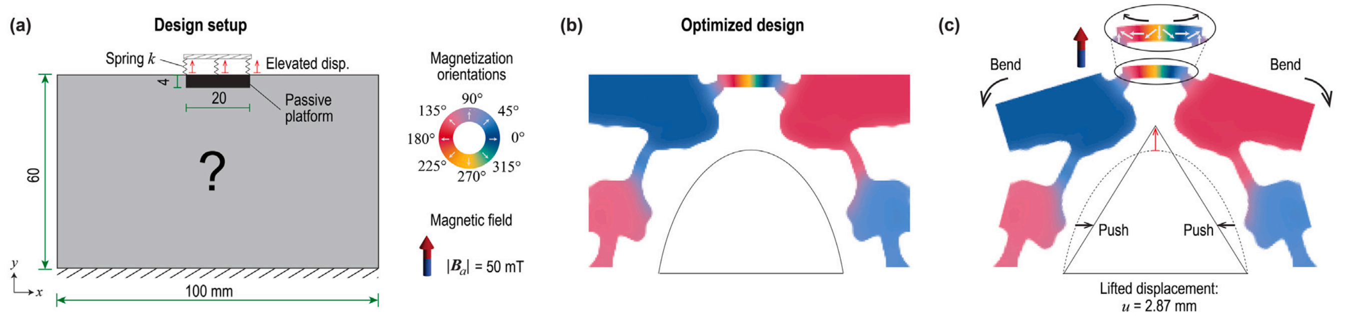

Fig. 6. Design setup and optimization of the magneto-active elevator. (a) Design domain, boundary conditions, and controlled displacements. (b) Optimized design without actuation. (c) Optimized design under a 50 mT vertical magnetic field, achieving a 2.87 mm central lift of the platform.

4.2.2. Magnetic property of the DIW printed hard-magnetic soft material

Unlike the uniform magnetizing approach, where the material is magnetized under an impulse magnetic field (2 T) after curing, which yields the maximum achievable residual magnetic flux density under the fixed volume fraction of NdFeB magnetic particles, the magnetic flux density of the DIW printed sample lies in the alignment of the particles with the printing direction. Specifically, it involves magnetizing the material first after mixing. An external magnetic field is applied to realign the magnetic particles within the liquid-state soft material, ensuring the magnetization direction aligns with the printing direction. Magnetic shielding is applied to prevent interference with the printed samples, and the material is cured in the final step. The actual magnetic flux density can be influenced by the applied magnetic field in two ways: if it is too weak, the particles may not align properly, reducing magnetization; if it is too strong, the magnetic shield may not function effectively, perturbing the alignment of the printed particles. Based on our experimental experience, we calibrated the magnetic field at the nozzle tip to 40 mT, with a post-shielding value in the range of 0.1 to 0.4 mT. To determine the actual magnetic flux density induced during the printing alignment, we printed magnetized sheets under the external magnetic field using a nozzle tip with an inner diameter of 0.41 mm and a printing speed of 5 mm/s. Samples (2 mm × 2 mm × 1 mm) were cut from the printed rectangular sheet and subjected to magnetization measurements using a vibrating sample magnetometer. To verify that the magnetization direction is aligned with the printing direction of the filament, we measured the magnetic flux density of the samples at various angular positions relative to the measurement axis of the vibrating sample magnetometer. The magnetic moment $\mathbf{m}_r$ of the sample is first measured. Then, we back-calculate the residual magnetic flux density by $\mathbf{B}_r = \mathbf{m}_r \mu_0 / V$, where μ_0 is the magnetic permeability, and V is the volume of the sample. The results are shown in Fig. 4(e). The rotation angle, denoted as θ, represents the orientation of the printed filament with respect to the measurement axis. The magnitude of the magnetic flux density reaches its maximum when the filament is aligned with the measurement axis ($\theta = 0$ or $180°$) and decreases as θ increases, reaching nearly zero when the filament is orthogonal to the axis. This confirms that the magnetization induced during printing is indeed aligned with the printing direction. Fig. 4(f) presents the measured magnetization hysteresis loop for the case where $\theta = 180°$. The magnetic field was applied in the following sequence: 0 T → 2 T → 0 T → −2 T → 0 T → 2 T. The magnetic flux density at the initial point (0 T) represents the value induced by the printing alignment. The maximum achievable value is indicated by the residual magnetic flux density after magnetic saturation. The measured DIW-printed magnetization is 42 mT under the 40 mT external magnetic field, while the maximum achievable value at the same concentration of NdFeB particles is 70 mT. The DIW-printed magnetization achieves approximately 60% of the maximum value, consistent with comparisons found in the literature [15].

5. Experimental and numerical results

In this section, we present three examples to illustrate the comprehensive framework encompassing design, toolpath preparation, printing, and experimental validation of DIW for hard-magnetic soft materials with optimized printing paths. The first example involves optimizing the topology and magnetization distribution of a 2D magneto-active elevator, showcasing the path generation process and demonstrating its experimental performance. In the second example, we optimize the magnetization of a metasurface with a prescribed geometry to achieve various out-of-plane deformations, demonstrating that different toolpath strategies applied to the same geometry can result in distinct motions. Finally, the third example extends the framework's application to metamaterials, showcasing its broader effectiveness.

5.1. Magneto-active elevator

The objective of the first example is to design a magneto-active elevator by optimizing both the geometry and magnetization orientation. The design setup is illustrated in Fig. 6(a). The size of the design domain is 100 mm by 60 mm with a thickness of 1.5 mm. The design domain is fixed at the bottom and discretized by a 200 × 120 finite element mesh under the 2D plane stress assumption. The objective is to lift the passive platform located in the middle top part with a size of 20 mm × 4 mm up under the magnetic actuation. The elevation platform is set as the passive zone during the optimization where the density is fixed and only the magnetization is optimized. To achieve this, we formulate the design objective as

$$J_1(\mathbf{u}) = \max_{\alpha \in \{1,\dots,N_\alpha\}} u_\alpha, \tag{8}$$

where u_α represents the displacement at the α-th degree of freedom (DOF), and N_α is the total number of control DOFs. The location of the controlled DOF and the direction of the movement are shown in Fig. 6(a). Springs are attached to the controlled DOF mimicking the stiffness provided by the external objects elevated. The stiffness of the spring is set as 0.05 N/mm based on the numerical experience. The volume fraction limit is set as 0.4. To eliminate thin members or thin connections, the stress constraint is considered with the stress limit set as 0.2 MPa. The external magnetic field is set as 50 mT in the vertical direction. The symmetric filter of the density and magnetization is applied because the design setup is symmetric. The characterized material properties and the measured magnetic flux density of the printed hard-magnetic

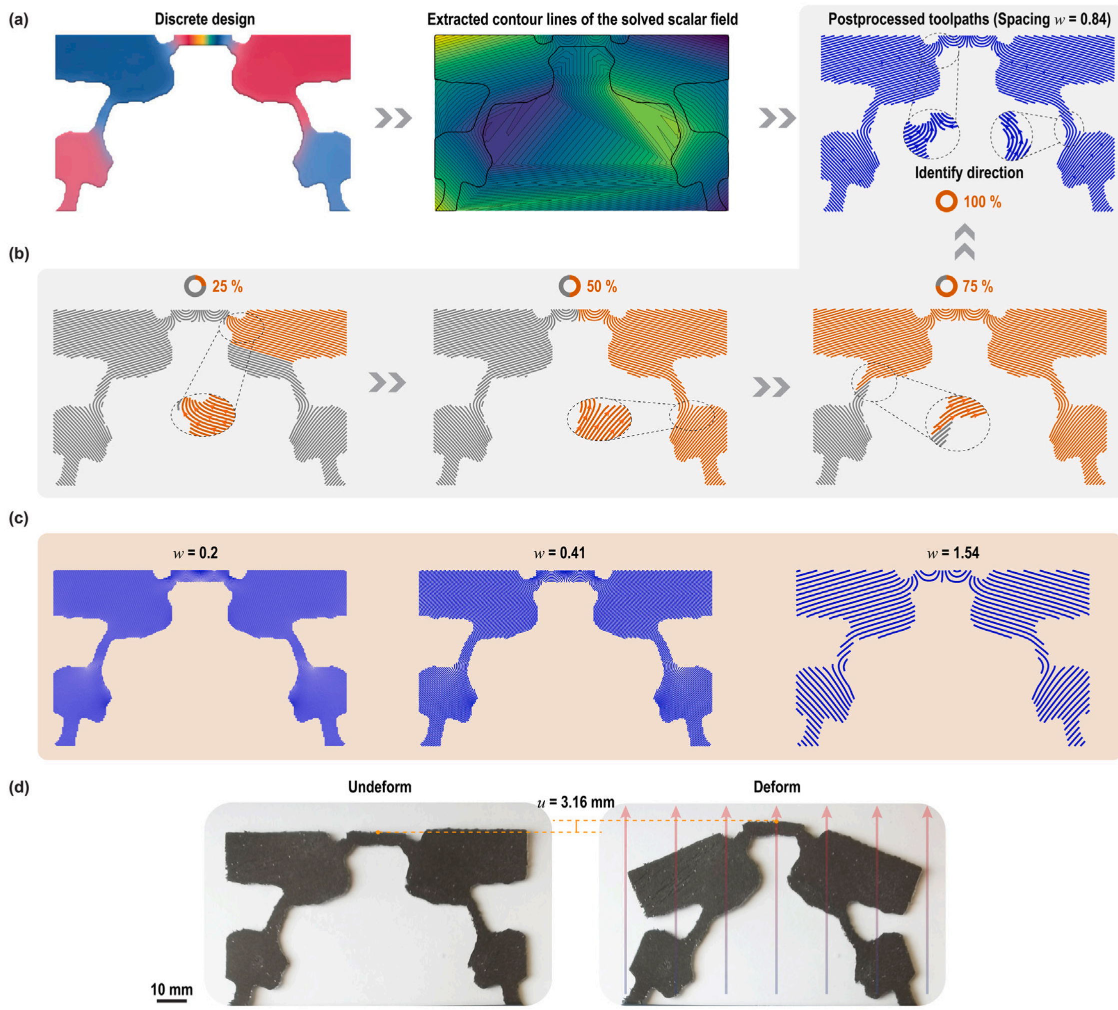

Fig. 7. Toolpath generation of the magneto-active elevator and the experimental validation. (a) Postprocessed discrete design, solved scalar field, and the extracted toolpaths with the spacing $w = 0.84$ mm. (b) Illustration of the printing sequence. (c) Toolpaths generated with various spacings of $w = 0.20$, 0.41, and 1.54 mm. (d) Experimental result of the printed design with the spacing $w = 0.41$ mm under an applied magnetic field $|\mathbf{B}_a| = 50$ mT in the vertical direction.

soft material are used for the finite element analysis: $\alpha_1 = 5.0625$, $\alpha_2 = -4.7973$, $\mu_1 = 0.3326$ MPa, $\mu_2 = 0.3039$ MPa, and $\mathbf{B}_r = 42$ mT.

The optimized design is illustrated in Fig. 6(b). The topology forms an arch-like shape, connecting four bulky blocks, with continuously varying magnetization throughout the structure. Under magnetic actuation (Fig. 6c), driven by magnetic torque, the bottom two blocks deform inward, reshaping the arch into a triangle and elevating the passive platform at the top. Simultaneously, the top two blocks bend, aligning the embedded magnetic particles with the external magnetic field, further lifting the central platform. The magnetization of the passive platform continuously changes from left to right, completing a full 360-degree variation in an anti-clockwise direction, starting and ending at 90°. This distribution allows the platform to bend inward, lifting the controlled points at the edge and balancing the movement of the entire platform.

Based on the optimized design, we explore toolpath generation and conduct experimental validation. First, the optimized design is post-processed into a discrete, solid-and-void format. Using the method introduced in Section 3, we solve for the scalar field v minimizing the global orientation energy (Eq. (6)), ensuring that its gradient approximates the orthogonal direction of the optimized magnetization. The extracted contour lines of the solved scalar field is shown in the second panel in Fig. 7(a) with redundant regions introduced by "`tricontour`", which are subsequently removed. We then adjust the start and end points of each contour line to align with the unidirectional magnetization direction. The final result is shown in the last panel in Fig. 7(a) with a contour spacing (level height) of $w = 0.84$ mm.

The printing sequence of the generated toolpaths is further adjusted to ensure adjacent toolpaths are printed consecutively by solving the TSP based on the distance between the start points of the current and remaining lines, d_{s-s}. Fig. 7(b) illustrates the printing sequence for a toolpath with a contour spacing of $w = 0.84$ mm. Once the global scalar field is obtained (Fig. 7a), toolpaths with different spacing parameters w can be easily generated by extracting contour lines at different contour heights. Fig. 7(c) demonstrates toolpaths generated with various spacings of $w = 0.20$, 0.41, and 1.54 mm, corresponding to different inner diameters of printing tips.

We then performed DIW of the optimized design using the toolpath generated with a spacing of $w = 0.41$ mm. The printing setup and parameters described in Section 4.1 were used. The fabricated sample is shown in Fig. 7(d). The design was printed successfully and the deformed shape under magnetic actuation closely aligns with the numerical results shown in Fig. 6(c). The experimentally measured lifted

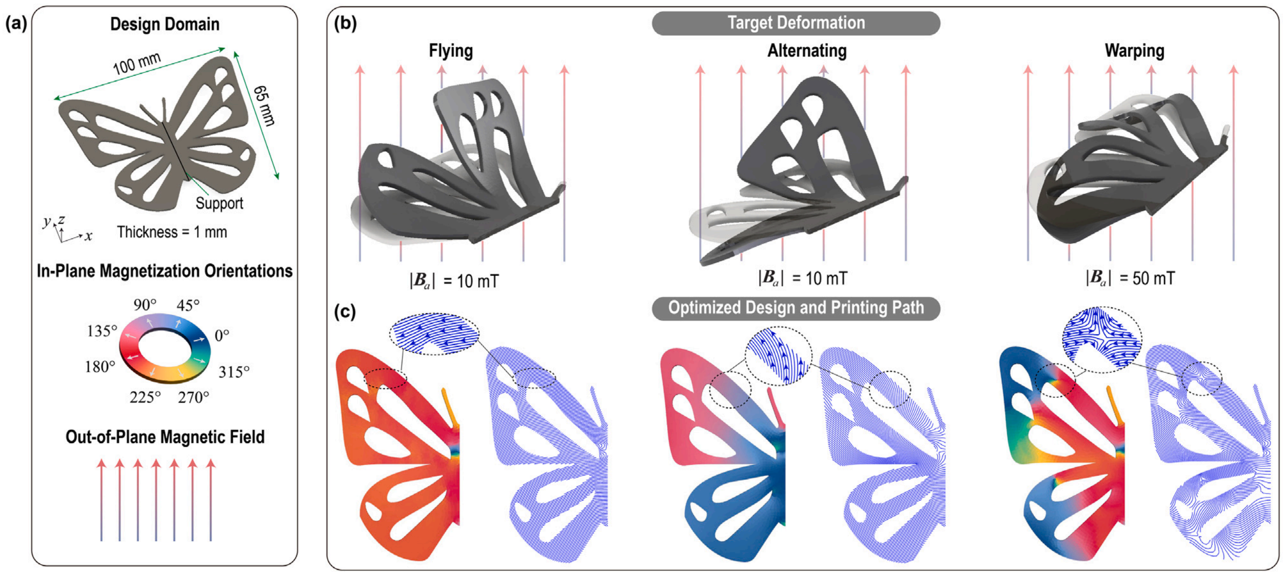

Fig. 8. Magnetic responsive butterfly with programmable deformation. (a) Design setup: design domain, candidate in-plane continuous magnetization orientations, and the prescribed external out-of-plane magnetic field. (b) Target deformation: "flying", "alternating", and "warping". (c) Optimized design and the corresponding printing path (spacing w = 0.41 mm).

displacement at the platform's central point is 3.16 mm, with a relative error of 10.1% compared to the numerical result.

5.2. Magneto-active metasurface

The DIW approach is particularly well-suited for fabricating sheet structures with out-of-plane deformation. In this example, we focus on the inverse design of a magneto-active metasurface. The goal is to program the continuous magnetization distribution for a given topology and generate corresponding toolpaths that achieve various desired deformations under external out-of-plane magnetic fields. This example showcases how different shape morphing can be encoded by slicing the same topology into different printing paths. To demonstrate the effectiveness of the proposed toolpath generation algorithm, we selected a butterfly-shaped design domain, featuring a complex geometry with multiple arbitrary inner holes discretized by an unstructured mesh.

The design setup is illustrated in Fig. 8(a). The butterfly's geometry is set to be symmetric, with its bottom surface fixed along the axis of symmetry. The out-of-plane thickness is set to 1 mm. The goal is to optimize the in-plane magnetization orientations under a prescribed out-of-plane magnetic field (applied in the positive z-direction) to achieve various out-of-plane deformations. The same optimization objective formulation in Eq. (8) is adopted. Given the symmetry of both the design domain and the target deformations, the optimization is conducted on a half-domain to reduce computational costs. Three target deformations are depicted in Fig. 8(b): "flying", where both the forewing and hindwing of the butterfly are lifted; "alternating", where the forewing is lifted while the hindwing is deformed downward; and "warping", where the butterfly's wings exhibit out-of-plane warping. The prescribed external magnetic fields for these scenarios are set at 10 mT, 10 mT, and 50 mT in the positive z-direction, respectively, based on numerical studies. The simulations are performed in 3D, with the design domain discretized using an unstructured mesh consisting of 8-node hexahedral finite elements. Given that the focus of the DIW process in this study is layered 2D printing, the magnetization orientations are mapped to be uniform along the thickness direction to ensure manufacturability. The characterized material properties are: $\alpha_1 = 5.0625$, $\alpha_2 = -4.7973$, $\mu_1 = 0.3326$ MPa, $\mu_2 = 0.3039$ MPa, and a residual magnetic flux density of 42 mT. To enhance numerical stability, the Poisson's ratio is set at 0.49.

The optimized designs and corresponding printing paths for the three scenarios, with spacing w set to 0.41 mm, are depicted in Fig. 8(c). The insets provide a zoom-in view of the toolpath directions. For the "flying" design, the optimized magnetization distribution is relatively uniform, with continuous directions oriented to the left. Under an upward out-of-plane magnetic field, the wings deform upward as the embedded magnetic particles align with the external field. This simple magnetization pattern results in a uniformly spaced printing path. In the "alternating" design, the forewing exhibits a continuous magnetization direction oriented to the left, while the hindwing's magnetization is continuously oriented to the right. This opposing alignment causes the wings to deform in opposite directions under magnetic actuation. The generated toolpaths reflect a seamless transition between these optimized continuous magnetization directions. For the complex "warping" shape, which is challenging to design intuitively, our framework effectively generates an optimized magnetization distribution that achieves the target deformation. Two singularity points, where the magnetization directions concentrate at a single location, are observed at the forewing and hindwing, respectively. This is expected for the warping deformation, as these internal points are designed to deform out-of-plane. Additionally, the optimized magnetization distribution is successfully mapped to the corresponding toolpaths using the proposed path generation algorithm. Due to the complexity of the geometry and magnetization distribution, the resulting printing path spacing in this design is less uniform, which may lead to overlaps or gaps during printing. This could be improved by balancing uniform spacing with precise alignment to the target vector in the global orientation energy. However, in this work, we prioritize alignment with optimized magnetization orientations. Experimental results indicate that despite the less uniform spacing, the printed products maintain high quality. In cases where large gaps occur, leading to disconnected features, the toolpaths can be effectively post-processed.

After generating the optimized toolpaths, we proceed with the DIW fabrication of the designs. Notably, it is straightforward to scale samples to various dimensions from the same design by updating the toolpaths accordingly. This involves simply scaling the input node information in the path generation algorithm while keeping other parameters unchanged. To illustrate the effortless scalability, Fig. 9(a) shows the sliced toolpaths for the "alternating" design at different scaling factors (1.3 and 2.0), with a path spacing parameter w set to 0.41 mm. From

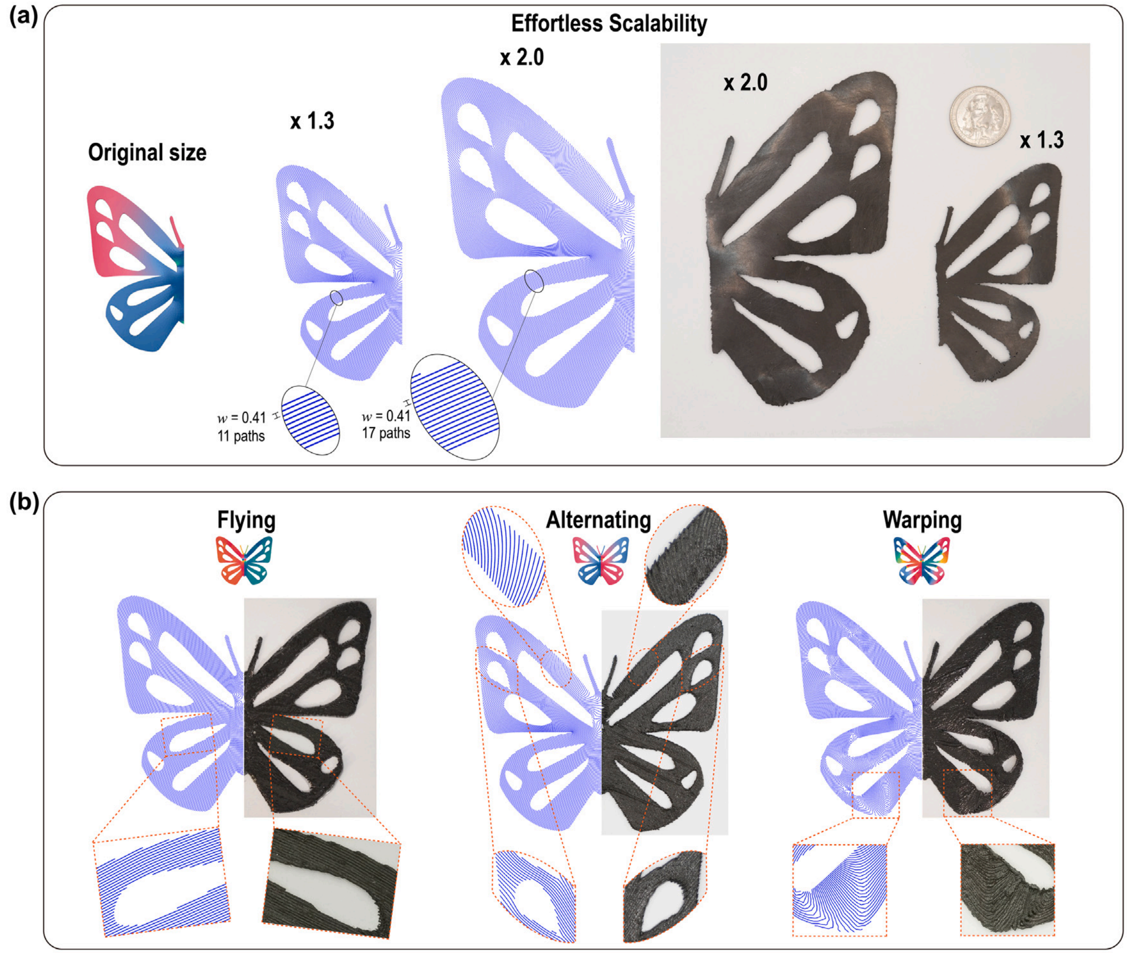

Fig. 9. DIW-printed magnetically responsive butterflies with optimized printing paths. (a) Printing paths for the scaled design at various scaling factors and the corresponding printed products, exemplified by the "alternating" encoded design. (b) DIW-printed samples exhibiting three distinct encoded shape morphing patterns at a scale factor of 1.3. The full-domain printing path is mapped from the symmetric half-domain design.

the zoom-in insets, we can see the toolpath spacing is consistent in these two cases while the number of toolpaths required to slice the same region increases with larger scaling factors. The fabricated samples for these scaled designs using a nozzle diameter of 0.41 mm are shown in Fig. 9(a), demonstrating that both samples can be successfully printed using the generated toolpaths.

In the subsequent experimental investigation, we consistently printed all three designs using a scaling factor of 1.3, which was found to offer the best printing quality and fit within our experimental space. Fig. 9(b) illustrates the toolpaths and the corresponding printed products. The zoom-in insets confirm that the designated toolpath pattern was accurately replicated in the physical samples. It is important to note that the optimization was performed on a half-domain design to reduce computational costs. To fabricate the complete design, we printed the two halves separately, with the printing path for the second half mirrored from the first. After printing and curing, the two halves were bonded together. However, we would like to emphasize that the entire domain could also be directly optimized to achieve a seamless transition in magnetization direction between the two halves. This approach would allow for integrated toolpaths to be generated, enabling the full design to be printed in a single process without the need for post-bonding.

The final fabricated samples for the three butterfly designs are shown in Fig. 10(a). Each printed sample has a thickness of 1.5 mm, achieved by printing three layers. We then conducted experimental validation using a Helmholtz coil to apply magnetic field actuation, with the experimental setup illustrated in Fig. 10(b). Fig. 10(c) presents the corresponding simulation results, modeled with the same dimensions as the printed samples. The external out-of-plane magnetic field was set to 25 mT, 25 mT, and 80 mT, respectively, to enhance the visualization of the deformed shapes. The experimentally observed deformed shapes are shown in Fig. 10(d) from both perspective and top views. The results demonstrate that the three target motions were successfully achieved by the printed samples. By slicing the same topology with different toolpaths, we effectively encoded different target deformations. The experimental outcomes generally align well with the simulation results, highlighting the effectiveness of the synthetic optimization and path generation framework.

5.3. Magneto-active metamaterial

In this example, we demonstrate the capability of the holistic framework in the design, path generation, and realization of the metamaterial. Fig. 11(a) presents the design setup. The design of the metamaterial is characterized by a 2D periodic unit cell with the plane stress assumption. The dimension of the unit cell is set as 30 mm × 30 mm × 1.5 mm for the length, height, and thickness, respectively. As shown in Fig. 11(a), the left bottom node is fixed, and we define the relative displacement $\triangle u_{ij}$ of the unit cell between the horizontal

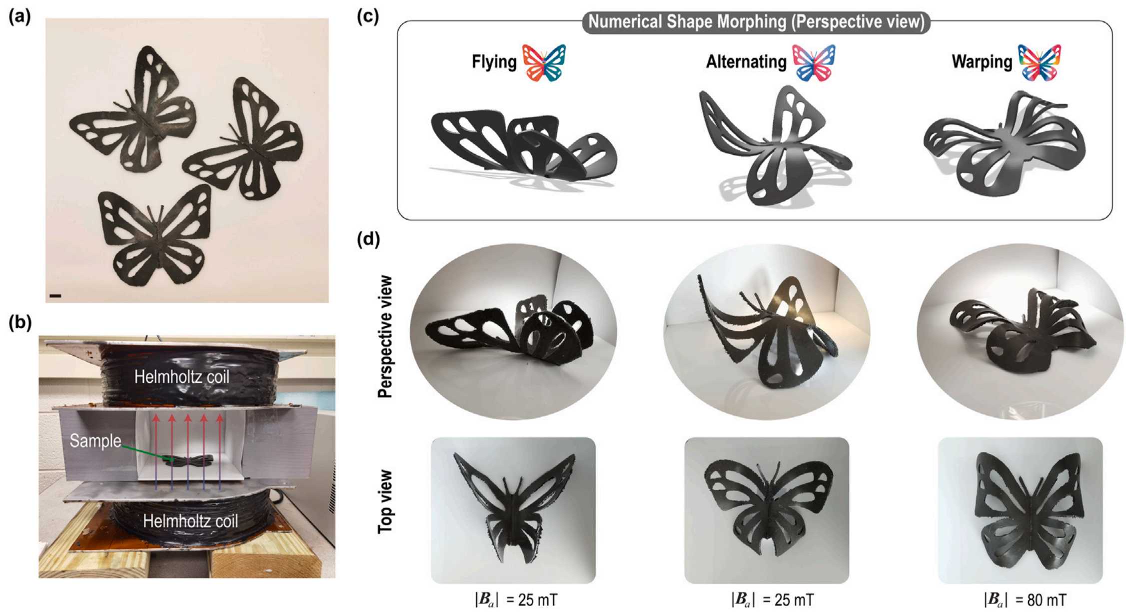

Fig. 10. Numerical and experimental demonstration of the three optimized butterflies. (a) Photograph of the three DIW-printed designs encoded with distinct optimized printing paths. Scale bar: 10 mm. (b) Experimental setup. (c) Numerical simulations of the three designs under prescribed out-of-plane magnetic fields. (d) Experimental demonstrations of the deformed shapes of the DIW-printed designs, presented from perspective and top views.

and vertical node pairs. For example, $\triangle u_{11} = u_{11} - u_{110}$, where u_{11} and u_{110} represent the x-direction displacements of the node pairs in the right and left boundaries, respectively. The design objective is to maximize the area shrinking under the magnetic actuation. The design formulation is expressed as

$$J_2(\mathbf{u}) = \max_{i,j}(w_{ij} \triangle u_{ij}), \quad i,j = 1,2 \tag{9}$$

where w_{ij} is the indicator of the direction of the displacement. To realize the area shrinking illustrated in Fig. 11(a), where the unit cell is compressed in both vertical and horizontal directions, we set $w_{11} = -1$, $w_{22} = -1$, and $w_{12} = w_{21} = 0$. In this example, we simultaneously optimize the density and magnetization distribution under the prescribed external magnetic field applied in the y-direction with the magnitude of 50 mT; The characterized mechanical and magnetic properties of the DIW-printed material are used (refer to Section 4). The periodic filtering is considered to ensure the continuous and smooth transition of the magnetization among different unit cells. The volume fraction and stress constraint limits are set as 40% and 0.1 MPa respectively. Fig. 11(b) shows the optimized unit cell. The area shrinking is achieved through the rotation of the four bulky blocks, driven by magnetic torque. The magnetization orientations vary continuously, with a seamless transition observed in the connecting members between the four blocks. Fig. 11(c) displays the 3 × 3 assembly, where the smooth transitions between individual unit cells are maintained.

Next, we generate integrated toolpaths for the 3 × 3 assembled metamaterial using the proposed path generation algorithm with the spacing parameter w set as 0.41 mm, as shown in Fig. 12(a). The minimum length $L < L_{\min}$ of the toolpath is set as 1 mm. The resolution of the segment size is set as 0.8 mm to improve the data loading efficiency for this large assembled metamaterial. The generated toolpaths are sorted according to the “start-to-start” distance d_{s-s}. We can see the generated toolpaths are uniformly spaced and align well with the optimized magnetization orientations. In the green-circled zoom-in figures, the printing path direction travels continuously within the individual unit cells. Furthermore, as shown in the orange-circled zoom-in figures, the toolpaths transition smoothly between different unit cells. Notably, the proposed method efficiently generates a global path for the entire assembled metamaterial in a single process, rather than simply repeating the path for individual unit cells, ensuring seamless transitions between different unit cells. Using the generated toolpath, we printed the assembled metamaterial and conducted experimental demonstrations. The printing parameters are detailed in Section 4. Magnetic actuation of $|\mathbf{B}_a| = 50$ mT is applied using a Helmholtz coil. The printed sample is placed on a plate with sand in between to reduce friction, and a clear polyethylene film is placed on top to prevent out-of-plane deformation. Fig. 12(b) presents the numerical and experimental results for the undeformed and deformed states. The printed sample aligns well with the numerical design, and the deformed shape closely matches the simulation, successfully achieving the area shrinking objective. The experimentally measured area reduction ratio is 23%, compared to 27% in the numerical results, resulting in a 14.8% error. A slight asymmetry in the experimental deformation is observed, primarily due to manufacturing imperfections during DIW printing. Nonetheless, the adopted printing parameters and experimental setup ensure a relatively good agreement between experiments and simulations.

6. Conclusions

This paper presents a comprehensive framework that integrates topology optimization with DIW of magnetic soft materials, enabling the encoding of continuous magnetization through optimal printing paths. From the design perspective, we extend the continuous hard-magnetic soft material optimization framework to consider manufacturing criteria and expand the design space to achieve 3D out-of-plane deformation via planar structures. A systematic toolpath generation algorithm is proposed to bridge design optimization [48,49] and additive manufacturing [50]. This method not only efficiently and accurately maps optimized magnetization directions to continuous printing paths while preserving the optimized topology, but also allows for flexible adjustment of path spacing to accommodate different printing head sizes and enables effortless scalability of fabricated products. The DIW process for hard-magnetic soft materials is detailed, complemented by a comprehensive discussion of key printing parameters. To validate our approach, we experimentally characterized the mechanical and magnetic properties of the printed materials. The framework's capabilities are demonstrated through three examples. In the first example, we present the design of a magneto-active elevator, optimized for

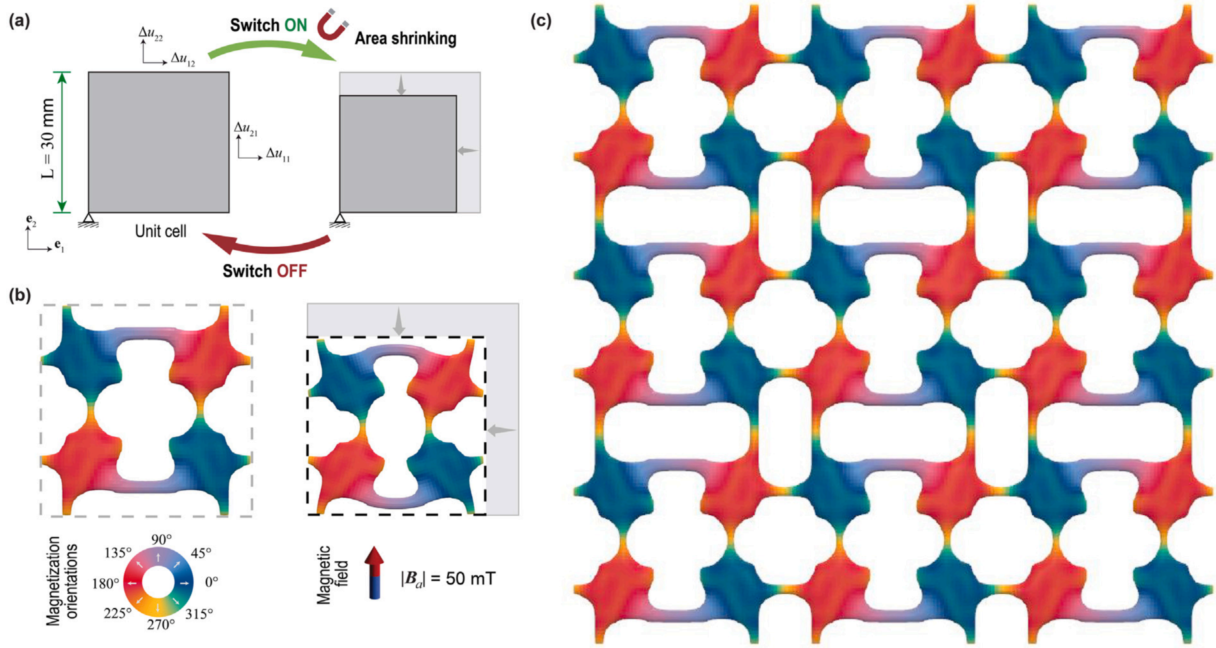

Fig. 11. Design setup and the optimized result of the magneto-active metamaterial programmed with area shrinking under magnetic actuation. (a) Design domain and periodic boundary conditions of the unit cell and the targeted area shrinking. (b) Optimized unit cell and the deformed configuration under a vertically applied magnetic field actuation of $|\mathbf{B}_a| = 50$ mT. (c) A 3 × 3 assembly of the optimized design.

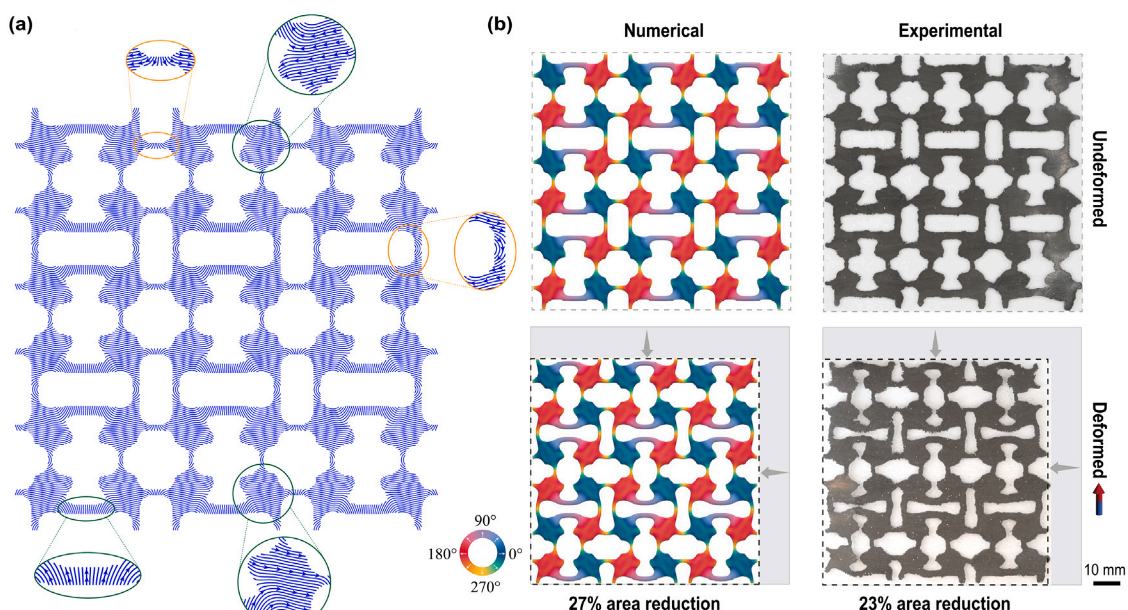

Fig. 12. Toolpaths, numerical simulations, and experimental demonstration of the 3 × 3 assembled metamaterial. (a) Integrated printing paths (spacing $w = 0.41$ mm). Green-circled zoom-in images highlight transitions within a unit cell, while orange-circled zoom-in images show transitions between adjacent unit cells. (b) Numerical simulations and experimental demonstrations of the assembly, with and without magnetic actuation ($|\mathbf{B}_a| = 50$ mT). Scale bar: 10 mm.

both magnetization and density, followed by a parametric study of the generated toolpaths, including printing sequence and spacing. The optimized design is successfully printed and experimentally validated under magnetic actuation. The second example showcases the design, fabrication, and experiment of "butterfly" metasurfaces with various continuous magnetization distributions, enabling different out-of-plane deformations under magnetic actuation. This example demonstrates how diverse shape-morphing behaviors can be encoded by manipulating the printing paths while maintaining a consistent topology. Finally, the third example focuses on a magneto-metamaterial, highlighting the framework's efficiency in generating a global toolpath for the entire assembled structure in a single process. This approach ensures seamless transitions between adjacent unit cells, advancing beyond the simple repeating of paths for individual cells.

Looking ahead, while this study primarily focuses on 2D and 3D out-of-plane deformations of planar magneto-active structures and metamaterials, extending the framework to full 3D space presents several challenges. From a design perspective, the increased computational cost and convergence issues in solving the 3D nonlinear problem can be significant, which require advanced parallel computing techniques and solvers. Additionally, fully 3D designs will introduce complex manufacturability constraints in the optimization, such as avoiding overhanging structures and ensuring continuous magnetizations across layers. Moreover, 3D magneto-active designs may exhibit strong self-interaction effects, potentially requiring fully-coupled magneto-mechanical models for accurate simulations [51]. From an experimental perspective, path generation must be adapted to accommodate variations in both shape and magnetization along the thickness direction, and printing stability remains a key challenge, potentially requiring support materials and advanced DIW techniques like multi-material deposition and adaptive extrusion parameters. Addressing these issues will require further advancements in computational modeling and experimental techniques, making this a critical area for future research. Moreover, expanding the framework to integrate multi-material design and fabrication presents another promising direction. The development of multimaterial DIW [14,16] enables the production of topology-optimized multi-material composites with tunable properties and functionalities. Furthermore, improvements to the path generation algorithm could address specific manufacturing requirements, such as balancing uniform toolpath spacing with alignment to vector orientations, and accommodating the bidirectional behavior of materials like LCEs. These advancements represent important directions for future work.

CRediT authorship contribution statement

Chao Wang: Writing – review & editing, Writing – original draft, Visualization, Validation, Software, Methodology, Investigation, Formal analysis, Data curation. **Zhi Zhao:** Writing – review & editing, Writing – original draft, Visualization, Software, Methodology. **Zeyu Li:** Writing – review & editing, Validation, Methodology, Investigation. **Yingqi Jia:** Investigation, Visualization, Writing – review & editing. **Arvin Ardebili Sharma:** Writing – review & editing, Investigation. **Xiaojia Shelly Zhang:** Writing – review & editing, Writing – original draft, Supervision, Resources, Project administration, Methodology, Investigation, Funding acquisition, Conceptualization.

Declaration of competing interest

The authors declare that they have no known competing financial interests or personal relationships that could have appeared to influence the work reported in this paper.

Acknowledgments

The authors acknowledge the financial support from the U.S. Defense Advanced Research Projects Agency (DARPA) Young Faculty Award (N660012314013), the U.S. National Science Foundation (NSF) CAREER Award (CMMI-2047692), and the U.S. NSF Award (CMMI-2245251). Testing of the rheological properties was carried out in part in the Materials Research Laboratory Central Research Facilities, University of Illinois. The information provided in this paper is the sole opinion of the authors and does not necessarily reflect the view of the sponsoring agency.

Appendix A. Interpolated magneto-mechanical free energy model

We use an interpolated magneto-mechanical free energy model to describe the nonlinear magneto-mechanical behavior of hard-magnetic soft materials under large deformation. This model is interpolated through the physical variables $\overline{\rho}(\mathbf{X})$ where $\mathbf{X}$ is a location vector in the reference configuration. This section provides a concise overview of the interpolated constitutive model. For a complete description of the model, the readers are referred to [26]. The interpolated free energy W_{I} is formulated as:

$$W_{\mathrm{I}}\left(\mathbf{u}, \overline{\rho}, \overline{m}^{(1)}, \overline{m}^{(2)}\right) = \left(\epsilon + (1-\epsilon)\overline{\rho}^{p_\rho}\right) W_{\mathrm{E}}(\mathbf{u}) + \overline{\rho}^{p_\rho} W_{\mathrm{M}}\left(\mathbf{u}, \mathbf{B}_{\mathrm{r}}(\overline{m}^{(1)}, \overline{m}^{(2)})\right), \tag{10}$$

where $\mathbf{u}$ is the displacement field (mapping from the reference to current configuration: $\mathbf{x} = \mathbf{X} + \mathbf{u}$). The power p_ρ is a penalization factor inspired by the SIMP (Solid Isotropic Material with Penalization) method [42] to promote $\overline{\rho}_e$ to adopt values of either 0 or 1. To mitigate numerical instabilities, a small value ϵ is introduced to avoid numerical singularities, and an energy interpolation scheme [52] is applied to the stored energy W_{E}.

For the hyperelastic stored energy W_{E}, we adopt an isotropic hyperelastic model, as described in Eq. (7). For 2D modeling, we use an incompressible model, and for 3D modeling, we apply a nearly incompressible model with additional terms related to the Jacobian J [47].

For the magnetic energy, we use a simplified model for hard-magnetic soft materials [53]. The magnetic energy in the reference configuration (per unit volume) is given by

$$W_{\mathrm{M}}(\mathbf{F}(\mathbf{u})) = -\frac{1}{\mu_0}\mathbf{F}\mathbf{B}_{\mathrm{r}} \cdot \mathbf{B}_{\mathrm{a}}, \tag{11}$$

where $\mathbf{B}_{\mathrm{r}}$ is the interpolated residual magnetic flux density, $\mathbf{B}_{\mathrm{a}}$ is the external magnetic flux density, and $\mathbf{F}$ is deformation gradient.

Upon using a standard displacement-based finite element method, we discretize the domain with N_e elements and N_n nodes. The total potential energy $\Pi(\mathbf{u}_v)$ and its stationary condition $\mathbf{r}(\mathbf{u}_v)$ are expressed in terms of the discretized mesh, where N_e represents the number of elements, as follows:

$$\Pi(\mathbf{u}_v) = \sum_{e=1}^{N_e} \int_{\Omega_e} W_{\mathrm{I}}(\mathbf{u}_v)\,\mathrm{d}\mathbf{X} - \left(\mathbf{f}_{\mathrm{ext}}\right)^{\mathrm{T}} \mathbf{u}_v, \tag{12}$$

and

$$\mathbf{r}(\mathbf{u}_v) = \frac{\partial \Pi}{\partial \mathbf{u}_v}(\mathbf{u}_v) = \mathbf{f}_{\mathrm{int}}(\mathbf{u}_v) - \mathbf{f}_{\mathrm{ext}} = \mathbf{0}, \tag{13}$$

where Ω_e refers to the mesh domain for each element, and $\mathbf{u}_v$ represents the displacement vector at the nodes. Additionally, $\mathbf{r}$ denotes the global residual, $\mathbf{f}_{\mathrm{int}}$ the internal force vector, and $\mathbf{f}_{\mathrm{ext}}$ the external force vector. The nonlinear equation in (13) is solved through the Newton's method.

Appendix B. Experimental testing of rheological properties of used inks

This section presents the testing of the rheological properties of used inks, including storage and loss shear moduli, viscosity, and relaxation time. Three groups of samples were evaluated: (1) non-magnetized ink, (2) magnetized ink (ink magnetized by a 2 T field), and (3) magnetized & aligned ink (ink magnetized by a 2 T field and subsequently realigned under a 40 mT magnetic field). All tests were conducted using the Discovery HR-3 rheometer (TA Instruments). As shown in Fig. 13(a), the rheometer consists of a rotatable stainless steel plate (diameter: 25 mm) on top and a fixed plate at the bottom. The sample is placed between these plates with a gap of 500 μm, which is 100 times the particle diameter (5 μm) of the used ink. After preparation, all samples were tested immediately at a constant temperature of 25 °C. The detailed testing procedures and results are outlined below.

Storage and loss shear moduli. To measure the storage and loss shear moduli, the rheometer applies torque to the rotatable plate, which then induces shear stress in the sample. The plate oscillates at a constant angular frequency of 2π rad/s with stress amplitudes increasing from approximately 10 to 2,500 Pa. The corresponding storage and loss shear moduli are recorded and shown in Fig. 13(b) and (c), respectively. Both moduli increase significantly after magnetizing but remain nearly unchanged after alignment.

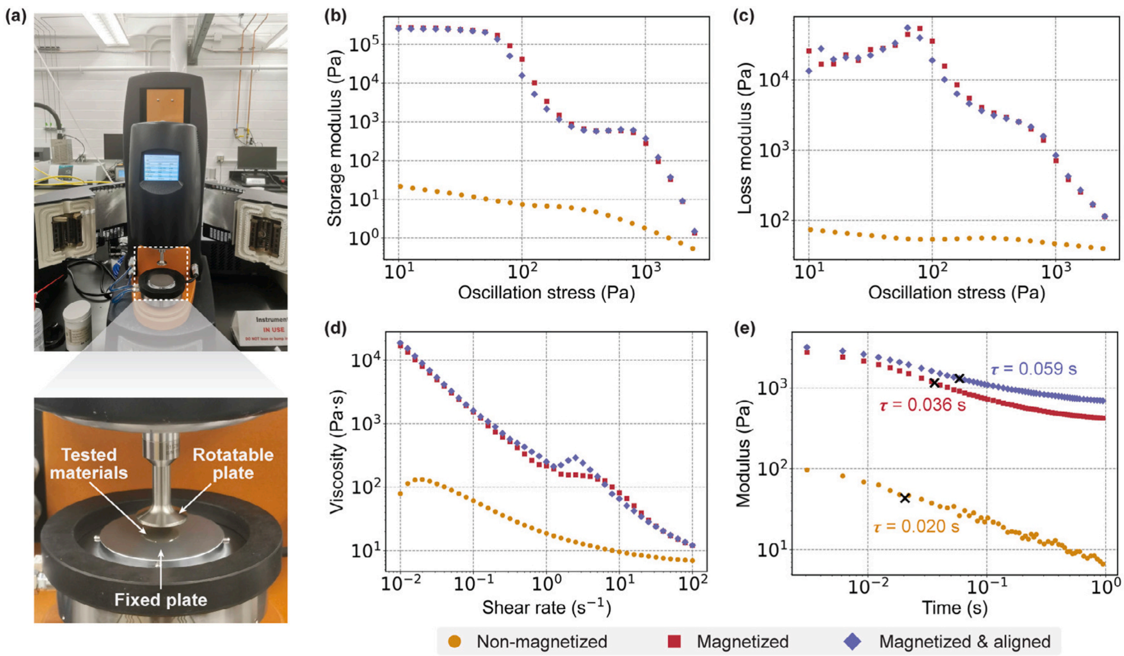

Fig. 13. Testing of rheological properties of used inks. (a) Testing setups. (b) Storage shear modulus. (c) Loss shear modulus. (d) Viscosity. (e) Relaxation time.

Viscosity. Viscosity measurements were performed by rotating the top plate unidirectionally under shear rates ranging from 10^{-2} to 10^{2} s^{-1}. The applied shear stress was recorded, and viscosity was calculated as the shear stress divided by the shear rate. The viscosity–shear rate relationship is shown in Fig. 13(d). The viscosity reduces with increasing shear rates, showing that the used ink is a shear-thinning material. Additionally, similar to the shear moduli trends in Fig. 13(b) and (c), viscosity increases after magnetization and remains stable after alignment.

Relaxation time. To determine the relaxation time, the rheometer rapidly rotated the top plate to induce a 20% shear strain. The strain was then held constant, and the relaxation modulus was recorded over time. The relaxation time (τ) was computed at the moment when the relaxation modulus dropped to $1/e$ of its initial value where $e \approx 2.72$ is the Euler's number. The computed values, marked in Fig. 13(e), show an increase from $\tau = 0.020$ s (non-magnetized ink) to $\tau = 0.036$ s after magnetization and $\tau = 0.059$ s after alignment.

Appendix C. Supplementary data

Supplementary material related to this article can be found online at https://doi.org/10.1016/j.addma.2025.104770.

Data availability

Data will be made available on request.

References

[1] X. Wan, L. Luo, Y. Liu, J. Leng, Direct ink writing based 4D printing of materials and their applications, Adv. Sci. 7 (16) (2020) 2001000.

[2] C. Zhang, X. Li, L. Jiang, D. Tang, H. Xu, P. Zhao, J. Fu, Q. Zhou, Y. Chen, 3D printing of functional magnetic materials: From design to applications, Adv. Funct. Mater. 31 (34) (2021) 2102777.

[3] J.W. Boley, W.M. Van Rees, C. Lissandrello, M.N. Horenstein, R.L. Truby, A. Kotikian, J.A. Lewis, L. Mahadevan, Shape-shifting structured lattices via multimaterial 4D printing, Proc. Natl. Acad. Sci. 116 (42) (2019) 20856–20862.

[4] M. Saadi, A. Maguire, N.T. Pottackal, M.S.H. Thakur, M.M. Ikram, A.J. Hart, P.M. Ajayan, M.M. Rahman, Direct ink writing: a 3D printing technology for diverse materials, Adv. Mater. 34 (28) (2022) 2108855.

[5] Y. Guo, Y. Liu, J. Liu, J. Zhao, H. Zhang, Z. Zhang, Shape memory epoxy composites with high mechanical performance manufactured by multi-material direct ink writing, Compos. Part A: Appl. Sci. Manuf. 135 (2020) 105903.

[6] Z. Tang, J. Gong, P. Cao, L. Tao, X. Pei, T. Wang, Y. Zhang, Q. Wang, J. Zhang, 3D printing of a versatile applicability shape memory polymer with high strength and high transition temperature, Chem. Eng. J. 431 (2022) 134211.

[7] W. Zhang, H. Wang, H. Wang, J.Y.E. Chan, H. Liu, B. Zhang, Y.-F. Zhang, K. Agarwal, X. Yang, A.S. Ranganath, et al., Structural multi-colour invisible inks with submicron 4D printing of shape memory polymers, Nat. Commun. 12 (1) (2021) 112.

[8] J. Sun, W. Liao, Z. Yang, Additive manufacturing of liquid crystal elastomer actuators based on knitting technology, Adv. Mater. 35 (36) (2023) 2302706.

[9] X. Peng, S. Wu, X. Sun, L. Yue, S.M. Montgomery, F. Demoly, K. Zhou, R.R. Zhao, H.J. Qi, 4D printing of freestanding liquid crystal elastomers via hybrid additive manufacturing, Adv. Mater. 34 (39) (2022) 2204890.

[10] G. Hu, B. Zhang, S.M. Kelly, J. Cui, K. Zhang, W. Hu, D. Min, S. Ding, W. Huang, Photopolymerisable liquid crystals for additive manufacturing, Addit. Manuf. 55 (2022) 102861.

[11] Z. Wang, N. Boechler, S. Cai, Anisotropic mechanical behavior of 3D printed liquid crystal elastomer, Addit. Manuf. 52 (2022) 102678.

[12] Z. Chen, D. Zhao, B. Liu, G. Nian, X. Li, J. Yin, S. Qu, W. Yang, 3D printing of multifunctional hydrogels, Adv. Funct. Mater. 29 (20) (2019) 1900971.

[13] Y. Cheng, K.H. Chan, X.-Q. Wang, T. Ding, T. Li, X. Lu, G.W. Ho, Direct-ink-write 3D printing of hydrogels into biomimetic soft robots, ACS Nano 13 (11) (2019) 13176–13184.

[14] J. Simińska-Stanny, M. Nizioł, P. Szymczyk-Ziółkowska, M. Brożyna, A. Junka, A. Shavandi, D. Podstawczyk, 4D printing of patterned multimaterial magnetic hydrogel actuators, Addit. Manuf. 49 (2022) 102506.

[15] Y. Kim, H. Yuk, R. Zhao, S.A. Chester, X. Zhao, Printing ferromagnetic domains for untethered fast-transforming soft materials, Nature 558 (7709) (2018) 274–279.

[16] C. Ma, S. Wu, Q. Ze, X. Kuang, R. Zhang, H.J. Qi, R. Zhao, Magnetic multimaterial printing for multimodal shape transformation with tunable properties and shiftable mechanical behaviors, ACS Appl. Mater. & Interfaces 13 (11) (2020) 12639–12648.

[17] Z. Wang, Y. Wu, B. Zhu, Q. Chen, L. Wang, Y. Zhao, D. Sun, J. Zheng, D. Wu, A magnetic soft robot with multimodal sensing capability by multimaterial direct ink writing, Addit. Manuf. 61 (2023) 103320.

[18] X. Zhang, H. Hu, D. Tang, C. Zhang, J. Fu, P. Zhao, Magnetic flexible tactile sensor via direct ink writing, Sensors Actuators A: Phys. 327 (2021) 112753.

[19] C. Ma, Y. Chang, S. Wu, R.R. Zhao, Deep learning-accelerated designs of tunable magneto-mechanical metamaterials, ACS Appl. Mater. & Interfaces 14 (29) (2022) 33892–33902.

[20] L. Wang, Y. Chang, S. Wu, R.R. Zhao, W. Chen, Physics-aware differentiable design of magnetically actuated kirigami for shape morphing, Nat. Commun. 14 (1) (2023) 8516.

[21] C. Wang, Z. Zhao, X.S. Zhang, Inverse design of magneto-active metasurfaces and robots: Theory, computation, and experimental validation, Comput. Methods Appl. Mech. Engrg. 413 (2023) 116065.
[22] Z. Zhao, C. Wang, X.S. Zhang, Tuning buckling behaviors in magnetically active structures: topology optimization and experimental validation, J. Appl. Mech. 90 (9) (2023).
[23] C. Wang, Z. Zhao, J. Han, A.A. Sharma, H. Wang, X.S. Zhang, Wireless magnetic robot for precise hierarchical control of tissue deformation, Adv. Sci. 11 (35) (2024) 2308619.
[24] S. Wu, J. Eichenberger, J. Dai, Y. Chang, N. Ghalichechian, R.R. Zhao, Magnetically actuated reconfigurable metamaterials as conformal electromagnetic filters, Adv. Intell. Syst. 4 (9) (2022) 2200106.
[25] S. Wu, C.M. Hamel, Q. Ze, F. Yang, H.J. Qi, R. Zhao, Evolutionary algorithm-guided voxel-encoding printing of functional hard-magnetic soft active materials, Adv. Intell. Syst. 2 (8) (2020) 2000060.
[26] Z. Zhao, C. Wang, X.S. Zhang, Multiphysics topology optimization of magnetic materials with continuous magnetization orientations, Mech. Mater. 198 (2024) 105089.
[27] Y. Jia, C. Wang, X.S. Zhang, FEniTop: a simple FEniCSx implementation for 2D and 3D topology optimization supporting parallel computing, Struct. Multidiscip. Optim. 67 (8) (2024) 140.
[28] Y. Jia, W. Li, X.S. Zhang, Multimaterial topology optimization of elastoplastic composite structures, J. Mech. Phys. Solids 196 (2025) 106018.
[29] G. Liu, W. Huang, Y. Wang, H. Ren, G. Zhang, L. Zhou, Y. Xiong, Stress field-aware infill toolpath generation for additive manufacturing of continuous fiber reinforced polymer composites, Mater. Des. 239 (2024) 112756.
[30] J.R. Kubalak, N.J. Root, A.L. Wicks, C.B. Williams, Improving mechanical performance in material extrusion parts via optimized toolpath planning, Addit. Manuf. 80 (2024) 103950.
[31] X. Chen, G. Fang, W.-H. Liao, C.C. Wang, Field-based toolpath generation for 3D printing continuous fibre reinforced thermoplastic composites, Addit. Manuf. 49 (2022) 102470.
[32] Y. Jia, K. Liu, X.S. Zhang, Unstructured growth of irregular architectures for optimized metastructures, J. Mech. Phys. Solids 192 (2024) 105787.
[33] D. Bommes, H. Zimmer, L. Kobbelt, Mixed-integer quadrangulation, ACM Trans. Graph. 28 (3) (2009) 1–10.
[34] J.P. Groen, F.C. Stutz, N. Aage, J.A. Bærentzen, O. Sigmund, De-homogenization of optimal multi-scale 3D topologies, Comput. Methods Appl. Mech. Engrg. 364 (2020) 112979.
[35] P.D.L. Jensen, O. Sigmund, J.P. Groen, De-homogenization of optimal 2D topologies for multiple loading cases, Comput. Methods Appl. Mech. Engrg. 399 (2022) 115426.
[36] Z. Guan, L. Wang, J. Bae, Advances in 4D printing of liquid crystalline elastomers: materials, techniques, and applications, Mater. Horizons 9 (7) (2022) 1825–1849.
[37] H. Jiang, C. Chung, M.L. Dunn, K. Yu, 4D printing of liquid crystal elastomer composites with continuous fiber reinforcement, Nat. Commun. 15 (1) (2024) 8491.
[38] Y. Wang, H. Ye, J. He, Q. Ge, Y. Xiong, Electrothermally controlled origami fabricated by 4D printing of continuous fiber-reinforced composites, Nat. Commun. 15 (1) (2024) 2322.
[39] T. Nomura, E.M. Dede, J. Lee, S. Yamasaki, T. Matsumori, A. Kawamoto, N. Kikuchi, General topology optimization method with continuous and discrete orientation design using isoparametric projection, Internat. J. Numer. Methods Engrg. 101 (8) (2015) 571–605.
[40] B. Bourdin, Filters in topology optimization, Internat. J. Numer. Methods Engrg. 50 (9) (2001) 2143–2158.
[41] F. Wang, B.S. Lazarov, O. Sigmund, On projection methods, convergence and robust formulations in topology optimization, Struct. Multidiscip. Optim. 43 (6) (2011) 767–784.
[42] M.P. Bendsøe, O. Sigmund, Topology Optimization: Theory, Methods, and Applications, Springer Science & Business Media, 2013.
[43] Z. Zhao, X.S. Zhang, Topology optimization of hard-magnetic soft materials, J. Mech. Phys. Solids 158 (2022) 104628.
[44] K. Svanberg, The method of moving asymptotes—a new method for structural optimization, Internat. J. Numer. Methods Engrg. 24 (2) (1987) 359–373.
[45] I.A. Baratta, J.P. Dean, J.S. Dokken, M. Habera, J.S. Hale, C.N. Richardson, M.E. Rognes, M.W. Scroggs, N. Sime, G.N. Wells, DOLFINx: The next generation FEniCS problem solving environment, 2023, http://dx.doi.org/10.5281/zenodo.10447666.
[46] ASTM-D412, Standard Test Methods for Vulcanized Rubber and Thermoplastic Elastomers-Tension, ASTM International, 2016.
[47] O. Lopez-Pamies, A new I1-based hyperelastic model for rubber elastic materials, Comptes Rendus Mec. 338 (1) (2010) 3–11.
[48] C. Wang, Z. Zhao, M. Zhou, O. Sigmund, X.S. Zhang, A comprehensive review of educational articles on structural and multidisciplinary optimization, Struct. Multidiscip. Optim. 64 (5) (2021) 2827–2880.
[49] Y. Jia, O. Lopez-Pamies, X.S. Zhang, Controlling the fracture response of structures via topology optimization: From delaying fracture nucleation to maximizing toughness, J. Mech. Phys. Solids 173 (2023) 105227.
[50] R.D. Kundu, X.S. Zhang, Additive manufacturing of stiff and strong structures by leveraging printing-induced strength anisotropy in topology optimization, Addit. Manuf. 75 (2023) 103730.
[51] K. Danas, P.M. Reis, Stretch-independent magnetization in incompressible isotropic hard magnetorheological elastomers, J. Mech. Phys. Solids 191 (2024) 105764.
[52] F. Wang, B.S. Lazarov, O. Sigmund, J.S. Jensen, Interpolation scheme for fictitious domain techniques and topology optimization of finite strain elastic problems, Comput. Methods Appl. Mech. Engrg. 276 (2014) 453–472.
[53] R. Zhao, Y. Kim, S.A. Chester, P. Sharma, X. Zhao, Mechanics of hard-magnetic soft materials, J. Mech. Phys. Solids 124 (2019) 244–263.